Title
Terahertz Saturable Absorbers

Author
Bloomfield, Jordane

Publication Date
2023

Peer reviewed|Thesis/dissertation

UNIVERSITY OF CALIFORNIA

Los Angeles

Terahertz Saturable Absorbers

A thesis submitted in partial satisfaction

of the requirements for the degree

Master of Science in Electrical and Computer Engineering

by

Jordane Antoinette Bloomfield

2023

ABSTRACT OF THE THESIS

Terahertz Saturable Absorbers

by

Jordane Antoinette Bloomfield

Master of Science in Electrical and Computer Engineering

University of California, Los Angeles, 2023

Professor Benjamin S. Williams, Chair

Semiconductor saturable absorber mirrors (SESAMs) are passive elements that have been used in tandem with lasers in the visible and infrared wavelengths to generate mode-locked pulses for applications in communication and spectroscopy. In this thesis, the simulation and characterization of terahertz saturable absorber metasurfaces and mid-IR samples embedded with quantum-cascade (QC) absorbing material are discussed. The reflectance of each design is simulated to determine expected saturation parameters and compared with analytic estimates. The characterization of the saturable absorber involves focusing a QC-vertical external cavity surface emitting laser (VECSEL) onto a saturable absorber in a reflection-mode spectroscopy configuration to measure the reflected power. Using a gold mirror as a reference, the reflectance is measured for frequencies near 3.4 THz at room temperature. Improvements to this experiment and a preliminary design for an external cavity incorporating a saturable absorber metasurface are proposed.

The thesis of Jordane Antoinette Bloomfield is approved.

Chandra J. Joshi

Sergio Carbajo Garcia

Benjamin S. Williams, Committee Chair

University of California, Los Angeles

2023

TABLE OF CONTENTS

LIST OF FIGURES

LIST OF TABLES

ACKNOWLEDGEMENTS

I would first like to thank my advisor, Professor Benjamin Williams, for his guidance throughout this project, especially during my mostly-remote first year at UCLA. I am greatly appreciative of the experience I've gained under his direction, and look forward to continuing work in the field. I'd also like to thank my lab mates for their advice: Yu Wu for transitioning me to this project and fabricating the saturable absorber samples, Anthony Kim for his assistance in optical alignment and training, Eilam Morag and Yue Shen for supervising my device testing, and Mohammad Shahili for his advice on active region simulation. I am especially thankful for their friendship. Finally, I would like to thank my friends, partner, and family for their unyielding encouragement.

VITA

2016-2020	B.S. in Electrical and Computer Engineering, University of Miami
2020-present	Graduate Student Researcher, Electrical and Computer Engineering, University of California, Los Angeles (UCLA)

Chapter 1

Introduction

1.1 Development of Saturable Absorbers

The generation of short, high intensity pulses in lasers through passive Q-switching, and later, mode locking, has been studied since the 60s [5, 6, 31, 29]. Ultrafast lasers are desirable for applications including communications, sensing, physics, and spectroscopy. For the latter, fast trains of ultrashort pulses are of particular interest as frequency comb (FC) sources. In the frequency domain, these pulses appear as evenly-spaced lines separated by the repetition rate of the laser [27, 17], making these particularly useful as precise frequency references. Saturable Absorber Semiconductor Mirrors (SESAMs) are intracavity elements used to passively generate frequency combs. These devices have been integrated in fiber and solid-state lasers from visible wavelengths to the infrared. However, these have yet to be integrated within the cavities of terahertz (THz) frequency lasers, although schemes for producing mode-locked THz pulses have been developed using femtosecond lasers [32].

1.1.1 Theory of Saturable Absorption

Early investigations of "giant pulse" formation via Q-switching include the theoretical analysis by Wagner and Lengyel, who modeled the evolution of a Q-switched pulse using rate equations and the work of Sooy, who determined that increased mode competition in passively Q-switched lasers led to single mode operation with narrowed linewidths [34, 30].

Szabo and Stein expanded the work of Wagner and Lengyel to saturable absorber-based Q-switching in ruby lasers, resulting in three normalized differential equations used to describe population inversion in the laser and absorbing media along with the photon density inside the cavity. From this analysis, the requirement for "giant pulse formation" was that the optical cross section of the saturable absorber must be greater than that of the laser medium. Generally, the larger the ratio of the two cross sections σ_s/σ_a, the higher the peak power output [33]. While this early approach provided numerical estimates for peak power and pulse width, a later closed-form analysis by Haus would generalize the impact of a saturable absorber on mode-locked pulses. The use of saturable absorbers in early experiments on Q-switched ruby lasers led to the simultaneous observation of passive mode locking, as Q-switching often resulted in emission of narrow linewidth pulse trains. Indeed, saturable absorber-induced mode locking was observed experimentally in passively Q-switched devices, independent of cavity lengths [22], and described theoretically by Haus in 1975 [10].

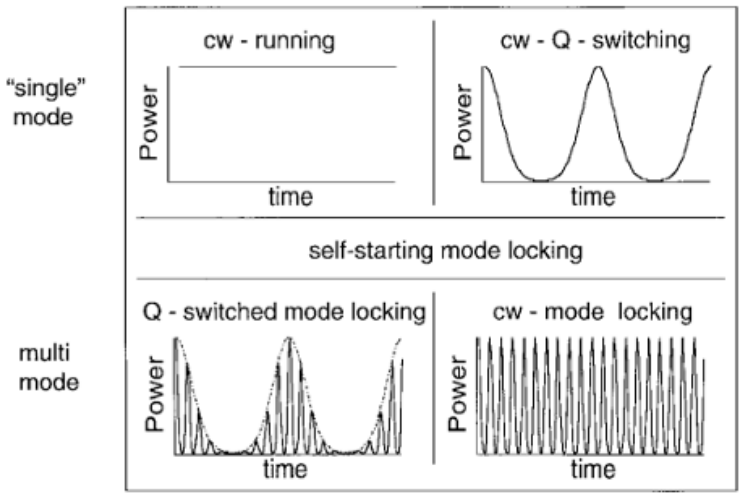

Figure 1.1: Figure from [16] highlighting pulse shape under different operating regimes.

Saturable absorbers work to create a very short net gain window in time. This occurs when the field interacting with the absorber is most intense, as then the nonlinear absorber is most reflective. Saturable absorbers are categorized as "fast" or "slow" depending on their

relaxation times relative to the duration of the pulse. Haus describes a laser medium with a fast saturable absorber in the time domain, introducing the effect of each component of the laser (gain medium, cavity, saturable absorber, mirrors) on the pulse individually, and assuming the net effect on the pulse after a round trip is zero (outside of a time delay). By this process, an operator is defined which accounts for the impact on the field of each component within the cavity:

$$\frac{-\omega_0}{2Q}[1 + \frac{Q}{Q_A(t)} - g(1 + \frac{1}{\omega_l^2})\frac{d^2}{dt^2} - \frac{1}{\omega_l}\frac{d}{dt}] \tag{1.1}$$

This term includes the linear cavity loss, $\frac{\omega_0}{2Q}$, the time-dependent modulation governed by the inverse Q of the saturable absorber ($Q_A(t)$): $\frac{Q}{Q_A(t)}$ the saturable gain g, and the dispersion ($(1 + \frac{1}{\omega_l^2})\frac{d^2}{dt^2}$) acquired by the time-delayed pulse, where the delay is given by: $\frac{1}{\omega_l}\frac{d}{dt}$. In steady-state conditions, this operator is set equal to 0. The rate equation:

$$\frac{\delta n}{\delta t} = -\frac{n - n_e}{T_A} - \sigma_A \frac{|v(t)|^2}{\hbar\omega_0 A_A} n \tag{1.2}$$

is used to define the inverse Q of the saturable absorber, which quantifies the energy loss within the cavity due to the saturable absorber relative to the cavity losses per round trip.

$$\frac{Q}{Q_A(t)} = q(1 - \frac{|v(t)|^2}{P_A}) \tag{1.3}$$

Since the loss associated with the saturable absorber is oscillatory in time, it will dominate the gain with some regularity. This has a modulating effect on the pulse. The small signal inverse q on the right hand side of the previous equation is given by:

$$q = \frac{2\sigma_A \theta_A A_A n_e}{\frac{\omega_0}{2Q} T_R}. \tag{1.4}$$

This term is derived from known or calculable values, like the absorber cross section, the thickness of the absorber, θ_A, the cross section of the beam on the absorber, A_A, the equilib-

rium population inversion, n_e, the amplitude of the envelope function $v(t)$, and the saturation power (or fluence) of the absorber, P_A. As are all other terms in this treatment of mode locking, the small-signal inverse q is normalized to the linear cavity loss $\frac{\omega_0}{2QT_R}$.

The resulting differential equation rewrites the operator defined above in terms of the small-signal gain and inverse Q, forming an equation similar to one describing a particle in a potential well:

$$[1 + q + (g + \delta)\frac{1}{\omega_L}\frac{d}{dt} - g(1 + \frac{1}{\omega_L^2}\frac{d^2}{dt^2})]v = q\frac{|v(t)|^2}{P_A}v \tag{1.5}$$

The solution takes the form:

$$v(t) = \frac{v_g}{cosh(\frac{t}{\tau_p})} \tag{1.6}$$

With the laser parameters being related by

$$\frac{1}{\omega_L\tau_p} \approx (\frac{g_0}{1+q} - 1)\frac{q}{1+q}\frac{P_L}{4P_A}\omega_L T_P, \tag{1.7}$$

where $\omega_L\tau_p$ is the product of the laser linewidth and pulse duration. When this relationship is graphed, it becomes clear that for a fixed excess gain term, small absorber saturation intensities (P_A) or a too-small Q yield multiple, unstable pulses within the cavity. Haus's condition to mode-locking with a saturable absorber is that the cavity round trip time, T_R, or gain recovery time, T_L, must be greater than the FWHM of the pulse, otherwise pulse overlap will lead to instabilities. The analysis of a slow saturable absorber differs from that of a fast saturable absorber in that the rate equations for the slow saturable absorber [11, 24] only include the contribution of the optical cross section of the saturable absorber (or the saturation fluence), and not on the relaxation time of the absorber. This slightly changes the definition of the inverse Q of the saturable absorber and thus the solution of the steady-state equation. The saturable absorbers presented in later sections of this thesis can best be modeled by the former solution because of the fast carrier dynamics of the quantum cascade architecture. Pump-probe measurements of THz QCLs have suggested gain recovery times

of tens of ps [1, 7]. However, changes to the master equation are necessary to account for the fast gain recovery times in both the saturable absorber and the gain medium:

$$[1 + q(1 - \frac{|v|^2}{P_A}) - g_0(1 - \frac{|v|^2}{P_{LF}}) - \frac{g_0}{\omega_L^2}\frac{d^2}{dt^2})]v = 0. \tag{1.8}$$

Above, P_{LF} is the saturation power of the fast gain medium. Stable mode locking is dependent on the relative scales of the dephasing times of the gain/absorbing media and the pulse width as these influence gain and absorption recovery times [15]. Haus assumes in the master equation approach that the relaxation time of the gain medium is long relative to the pulse duration and is effectively time-independent. For a fast gain medium, no solutions exist above threshold. Based on this formalism, a laser with a fast gain medium coupled with a fast saturable absorber would not be able to "self-start" mode locking.

1.1.2 Saturable Absorbers in Solid State Lasers, SESAMs

"SESAMs," or Semiconductor Saturable Absorber Mirrors, were first realized in the early 90s in ND:YLF lasers, although the acronym was adopted later. These devices were designed to fill the need for saturable absorption of solid-state lasers. It was thought that stable mode-locked pulses were not possible to produce via saturable absorption in solid-state lasers because of the longer ($\approx$ μs) gain relaxation times—a saturable absorber was required to shorten the net gain window enough to prevent Q-switched operation. To create a fast absorber, multiple-quantum well structures (MQWs) with shorter relaxation times were used. The interband transitions within III-V MQW structures is on the order of a nanosecond, but with the introduction of trap states, picosecond-scale recombination is possible. The first saturable absorber cavity designs were resonant coupled cavities to reduce the losses induced by the presence of a saturable absorber element. Later designs sandwiched or backed the saturable absorber with reflective layers (i.e., Bragg mirrors) to remove the coupled cavity constraint. The Bragg mirrors allowed the reflectivity of the absorber to be engineered to

meet a desired need. Also, the depth (d) of the absorber tunes the resonance of the device via

$$\phi_{rt} = \phi_{mirror,\,bottom} + \phi_{mirror,\,top} + 2knd = (2m+1)\pi, \tag{1.9}$$

where m is an integer [16].

Generally, higher reflectance is associated with high saturation fluence. Modern SESAMs can have either top and bottom mirrors, anti-reflective coatings, or no top mirrors at all to tune dispersion and reflectance. Already, these have been used to passively mode lock solid-state and fiber lasers from the visible to the MIR regions ($\approx 3\,\mu$m to ≈ 600 nm). [16] [25]. In 2004, Haiml, Grange, and Keller described the optical characterization of SESAMs to determine saturation fluence, modulation depth, and non-saturable losses [8]. The methods used to predict these parameters in a QC-metasurface-based saturable absorber were derived from these approaches and described in later sections. SESAMs have also been demonstrated in Kerr lens mode locking (KLM) and soliton mode locking systems [16].

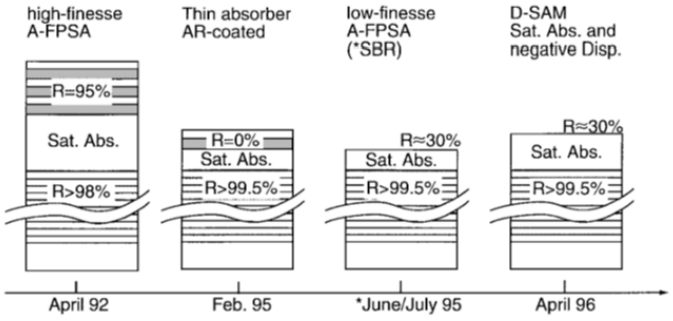

Figure 1.2: Examples of SESAM designs over time. [16].

1.2 Terahertz Technologies and applications

The terahertz frequency range is generally defined as 0.3 THz to 10 THz. This band of frequencies is traditionally known as the "terahertz gap" because there are fewer sources and detectors available. That said, this range is of interest for its applicability in communications, imaging, sensing, and research. Current methods of generating terahertz radiation include

photomixing between two lasers that generate a THz beatnote, photoconductive antennas (PCAs), and, notably, quantum cascade lasers (QCLs).

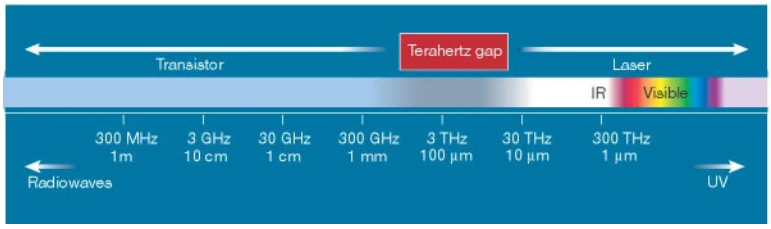

Figure 1.3: Electromagnetic spectrum with Terahertz band highlighted, from [28].

1.2.1 The Terahertz QC-VECSEL

Quantum cascade lasers (QCLs) are semiconductor devices whose lasing frequencies are determined by intersubband transitions (ISBTs) that take place entirely within quantum wells in the conduction band of the laser gain material, usually composed of III-V heterostructures grown using epitaxial methods to precisely tune the THz emission over large bandwidths [35]. Single ridge devices emit from the edge of the device in accordance with intersubband selection rules, but in 2015, the QC-vertical external cavity surface emitting laser (QC-VECSEL) was introduced by the Terahertz Devices and Intersubband Nanostructures Lab at UCLA.

The QC-VECSEL consists of a metasurface reflector housing the gain material and an output coupler mirror with frequency dependent reflectivity (generally near unity). The metasurface is a reflectarray of metal-metal waveguide-based ridges or patches sandwiching QC gain material. The ridges or patches act similarly to microstrip antennas [2] [14], which couple the lateral TM_{0x} waveguide mode to the external cavity mode to promote vertical emission. The cutoff frequency can be varied by changing the ridge widths by $\nu_0 = c/2nw_r$. Because the ridges are loaded with gain material, they also serve as amplifiers. The QC-VECSEL is electrically biased such that only an isolated circular bias area receives gain. The laser's output power scales with the bias area, and a smaller area generally implies less power consumption and heating. In order to avoid diffractive losses and self-lasing, the periodicity of the metasurface is kept below the designed wavelength of the radiating beam.

This improves beam quality relative to single ridge devices while maintaining near-Watt level output powers.

Frequency tunability is another advantageous feature of QC-VECSELs. The output coupler mirrors used for our QC-VECSELs are generally mounted on a piezoelectric stage, enabling us to lengthen the cavity and tune the output frequency of the lasers over the free spectral range. This was of particular importance for saturable absorber characterization, as QC-VECSELs were used as sources for reflectance measurements of our saturable absorber designs. The external cavity also enables the introduction of passive elements like saturable absorbers [36].

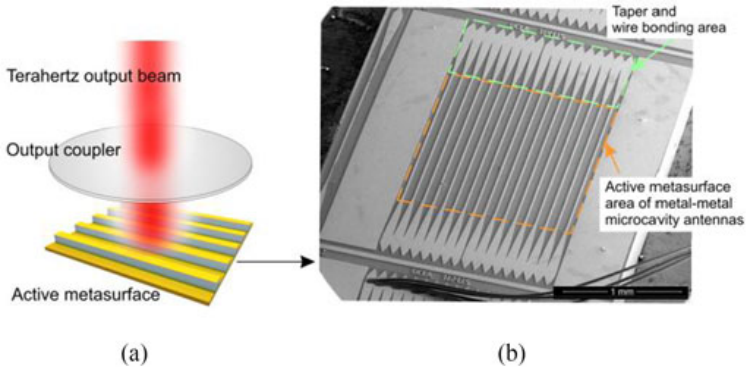

Figure 1.4: (a) Model of a QC-VECSEL with output coupler; (b) SEM image of a QC-VECSEL metasurface, from [36].

1.2.2 Mode Locking in QCLs

N-type semiconductors, graphene, and multiple quantum well (MQW) structures have been investigated with THz time-domain spectroscopy as possible candidates for passive mode locking. Recent results suggest pulse shortening of THz radiation and nonlinear saturation behaviors. Work from Raab, et al. on 2D THz spectroscopy projects relaxation times of 5ps in GaAs/AlGaAs MQW systems, shorter than gain recovery times of QCLs [26]. Although passive mode locking remains difficult to achieve, active mode locking has been demonstrated through a variety of means, usually through RF injection or injection locking. RF injection locking of THz QCLs has been exercised for years to investigate spectrum broadening. Mod-

ulating the gain of a laser near the round trip frequency creates side lobes in the spectrum and has already been applied to frequency comb generation [16, 12]. Broadening the laser spectrum via RF injection lends to the generation of ultrashort, mode-locked pulses in that the pulse width is inversely proportional to the bandwidth of the spectrum envelope [18]. Injection seeding is a phase-locking mechanism generally involving the use of a femtosecond laser and a photoconductive antenna (PCA) to generate terahertz radiation. The terahertz pulses generated using the PCA are used to fix the phase of the QCL while above threshold [23].

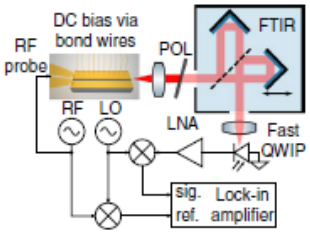

Figure 1.5: Example of an RF injection locking scheme, image from [12].

Chapter 2

Active Region and Metasurface Simulations

2.1 Schrödinger Equation Solver using Shooting Method

Understanding the gain dynamics of a saturable absorber generally requires two steps: the first being the determination of the wave functions for the states of interest. The second step is to calculate the time evolution of the population inversion within the active material using the wavefunctions calculated in the first step. The quantum cascade active region design used for the saturable absorber samples to be discussed were first simulated using MATLAB software by solving the time-independent Schrodinger equation for a single period. The numerical solution to the Schrodinger equation for these quantum wells followed a shooting method described by Harrison and Valavanis [9]. In this approach, derivatives are approximated using finite-difference forms to discretize the time independent Schrodinger equation:

$$-\frac{\hbar^2}{2m*}[\frac{\psi(z+\delta z)-2\psi(z)+\psi(z-\delta z)}{(\delta z)^2}]+V(z)\psi(z)=E\psi(z) \tag{2.1}$$

Upon discretization, the wavefunctions of each eigenstate are computed using the shooting method. The shooting method takes two "known" values of the wavefunction, $\psi(z-\delta z)$ and $\psi(z)$, and uses those to compute $\psi(z+\delta z)$:

$$\frac{\psi(z+\delta z)}{m^*(z+\delta z/2)}=\frac{2(\delta z)^2}{\hbar^2}[V(z)-E]+\frac{1}{m(z+\delta z/2)}+\frac{1}{m^*(z-\delta z/2)}\psi(z)-\frac{\psi(z-\delta z)}{m^*(z-\delta z/2)}. \tag{2.2}$$

This equation has been adjusted to account for the varying electron effective mass along each material of the active region. The effective mass is determined by averaging the effective mass a step ahead and a step behind in position.

Taking this equation and solving for $\psi(z + \delta z)$, generalized starting conditions of $\psi(z - \delta z) = 0$ and $\psi(z) = 1$ are used to iteratively solve for the wavefunctions over the entire period of the active region. These ensure that the boundary condition requiring exponential growth of the wavefunction between the barriers and wells is met. In certain designs, the inclusion of non-parabolic effective mass adjustments can be accounted for. This was applied to the THz and MIR active regions simulated in the following subsection.

The magnitudes of the eigenenergies associated with each subband energy level were found by checking whether the wavefunction converged at the farthest edge of the potential, V(z), for a range of energies within the wells. These rough estimates of the eigenenergies were used to recursively calculate new wavefunctions and more accurate energies. The final eigenstates and eigenenergies were applied to scripts that solve for the subband populations, calculate oscillator strengths, and estimate an absorption coefficient for a given active region. The population of each subband is calculated for the unbiased active region at a given temperature using a Fermi-Dirac distribution:

$$f(E) = \frac{1}{\exp[(E - E_F)/k_B T] + 1}, \tag{2.3}$$

Where E_F is the Fermi energy of the dopants, k_B is Boltzmann's constant, and T is the temperature in K. The simulated absorption coefficient for each design was calculated as a function of frequency using the following Lorentzian lineshape function:

$$\gamma(\nu) = \frac{\Delta\nu/2\pi}{(\nu - \nu_0)^2 + (\Delta\nu/2)^2}, \tag{2.4}$$

and the well-known gain equation:

$$g(\nu) = \frac{2\Delta N e^2 \nu_0 f_{i\to f}}{4m^* cn\epsilon_0}\gamma(\nu), \tag{2.5}$$

where ΔN is the 3D population inversion density and $f_{i\to f}$ is the oscillator strength of the transition of interest [35]. In these cases, the full-width at half-maximum (FWHM) is estimated as $\Delta\nu = \frac{1}{2\pi\tau_1} + \frac{1}{2\pi\tau_2} + \frac{1}{\pi T_2^*}$, where T_2^* is a phenomenological pure dephasing time, and the scattering rates are calculated using Fermi's Golden Rule:

$$W_{if}(k_i) = \frac{2\pi}{\hbar}\sum_{k_f} |< f|H(\boldsymbol{k}_i, \boldsymbol{k}_f)|i >|^2 \delta(E_f - E_i \pm \hbar\omega). \tag{2.6}$$

Here, k_i and k_f denote the wave vectors of the initial and final states, and H is the Hamiltonian associated with the interaction.

The broadening of the gain/absorption in the case of these absorbers is due to intrasubband scattering events associated with electron-phonon, electron-impurity, interface roughness, and electron-electron scattering. Because of the complexity, I assigned a phenomenological value for the broadening. This $\Delta\nu$ is estimated differently for the two absorber designs, as estimating the pure dephasing time in each requires more computationally expensive simulation.

2.1.1 SW66 - 10 Micron Design

The SW66 design, named so for its stack of 66 single-well $Al_{0.25}GaAs_{0.75}$/GaAs periods featuring a single transition of 115 meV, was used as a proof-of-concept for early multi-bounce transmission measurements at room temperature. The well width is 8 nm, and barrier widths of 220Å were used for computing the wavefunctions.

At 26.5 THz ($\sim$ 11.3 μm wavelength), the absorption coefficient α is 45 cm^{-1} at 300 K and 156 cm^{-1} at 0 K. $\Delta\nu$ was estimated to be $\approx$ 2.5 THz, since the absorption resonance is

relatively far from the LO phonon frequency in GaAs.

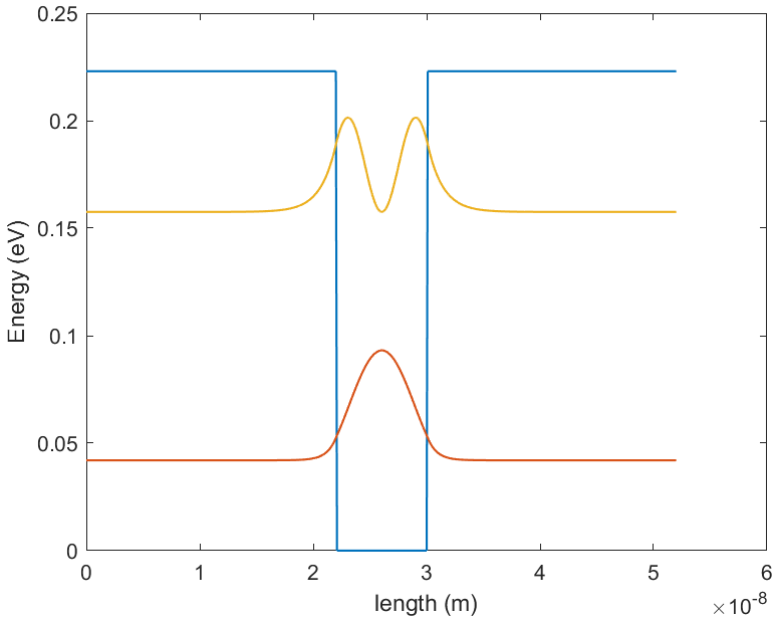

Figure 2.1: Band diagram of SW66 ISB absorbing region with wavefunctions

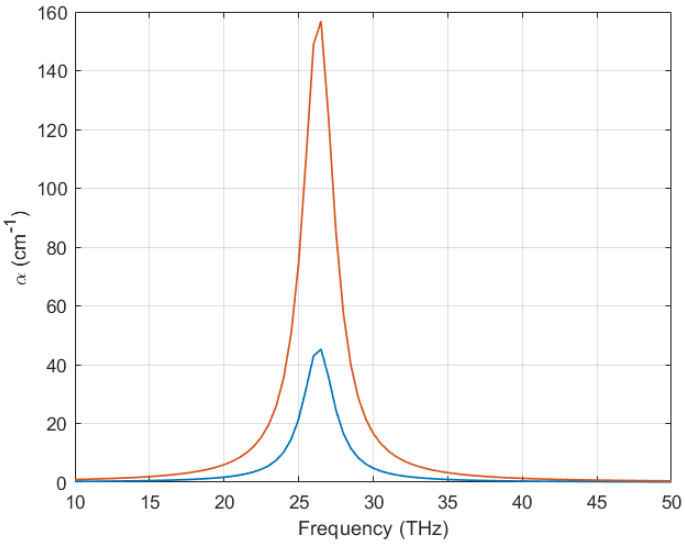

Figure 2.2: SW66 absorption coefficient calculated using, using subband populations calculated with a Fermi distribution at T = 300 K and at T = 0 K.

Table 2.1: Table of parameters used in active region calculations at $T = 300\,\mathrm{K}$.

	DW100	SW66
Fraction Al	0.1	0.25
$n_{eff,GaAs}$	3.6	3.3
$n_{eff,AlGaAs}$	3.25	3.17
Conduction Band Offset (meV)	89.2	223
Average Doping (cm^{-3})	2.82×10^{15}	1.33×10^{16}

2.1.2 DW100 - 3.4 THz Design

The DW100 design consists of 100 repetitions of a double-well ($Al_{0.10}Ga_{0.90}As$/GaAs) active region with barrier thicknesses of 220Å , 11 Å, and 749Å, and well thicknesses of 141Å and 99Å, resulting in a 10 micron thick active region. The doping density was 2.6×10^{16} cm^{-3}. The 2 to 1 transition was designed to be near 14 meV, or nearly 3.4 THz. The middle barrier is placed to increase interface scattering. This ISB region was used in the saturable absorber metasurfaces fabricated for testing. The 3.4 THz frequency was chosen to match with the frequency of the highest-performing QC-VECSEL lasers in the Williams group.

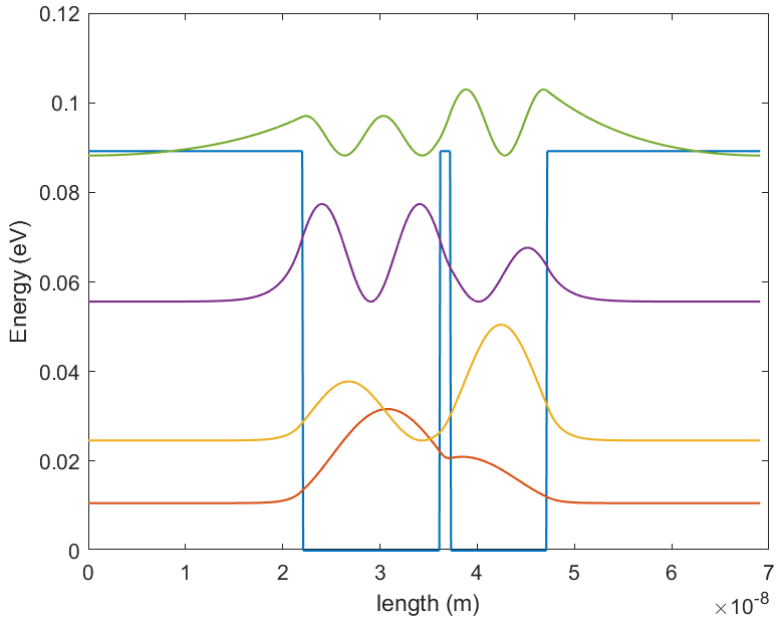

Figure 2.3: Band diagram of DW100 ISB absorbing region with wavefunctions

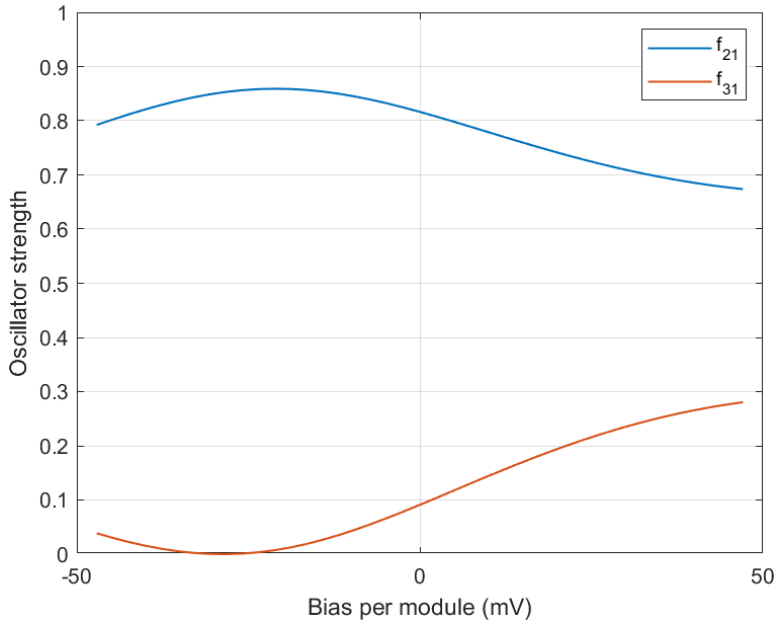

Figure 2.4: Oscillator strength as a function of bias for DW100 ISB absorbing region

Similarly to the SW66 design, the simulated absorption coefficient was calculated as a function of frequency. For the parameters in Table 2.1, at 3.39 THz the absorption coefficient is 68cm^{-1}. The absorption spectrum plotted in Fig. 2.5 takes into account the population

difference of the first and second subbands at equilibrium using a Fermi distribution at T = 300 K and at T = 0 K . These results will be compared to metasurface simulation results in the following sections.

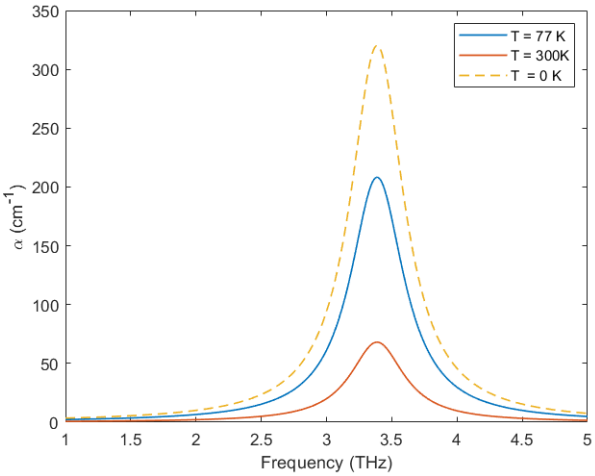

Figure 2.5: The absorption coefficient in cm^{-1} of the DW100 absorber calculated using the gain equation. Assuming the active region is fully relaxed at 0 K ($\Delta N = N$), when loss is greatest, for T = 77 K, and when the active region is in equilibrium at 300 K. The 300 K peak of 68 cm^{-1} and the 0 K peak of 320 cm^{-1} occur at 3.39 THz.

2.2 Linear Modeling of Metasurface Absorbers

The linear behavior of the saturable absorber can be described by characterizing the transparency gain, g_{tr}, the quality factor, Q, and the effective interaction length, ξ, a value closely related to the quality factor. The transparency gain represents the gain required for the metasurface to change from an absorbing surface to an amplifying one. The reflectance is modeled as a function of gain in COMSOL, where the linear gain is added to the relative permittivity via

$$\epsilon_{gain} = i[g_{uniform}\sqrt{\epsilon_{GaAs}}\frac{c}{2\pi\nu}], \tag{2.7}$$

where $g_{uniform}$ is the uniform gain applied to the ISB material. This term is only added to the relative permittivity to calculate the transparency gain and ξ, and is not present when modeling the nonlinear metasurfadce response. Both g_{tr} and ξ can be calculated by

fitting the reflectance at resonance of the metasurface as a function of gain to a straight line, and finding the point at which the reflectance is unity. ξ is a fitting parameter and is evaluated using MATLAB. This value is also important when calculating the saturation intensity, as will be discussed in the following sections. By simulating the metasurface without any intersubband loss contribution in the semiconductor, the nonsaturable losses of the metasurface are extracted. For the 75 µm period design, the unsaturable reflectance, R_{ns} is 0.145 at 3.39 THz. This corresponds to a nonsaturable absorption coefficient $\alpha_{ns} \approx 109\,\mathrm{cm}^{-1}$.

2.2.1 Determining Transparency Gain, ξ

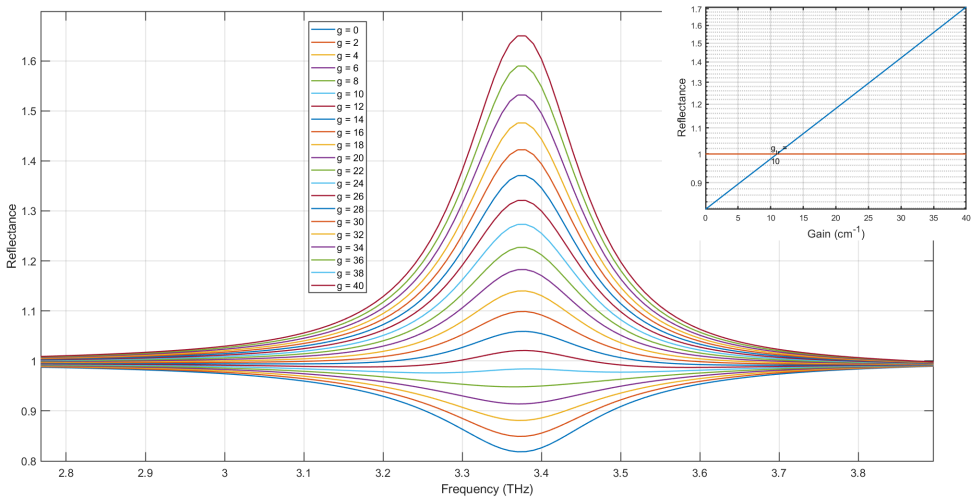

Figure 2.6: Reflectance of DW100 ridge metasurface saturable absorber versus gain, assuming $\tau_{||,GaAs} = 0.3\,\mathrm{ps}$. Inset: Minimum reflectance of DW100 ridge metasurface saturable absorber versus gain, assuming $\tau_{||,GaAs} = 0.3\,\mathrm{ps}$. From this graph, the transparency gain is calculated to be $g_{tr} = 10\,\mathrm{cm}^{-1}$.

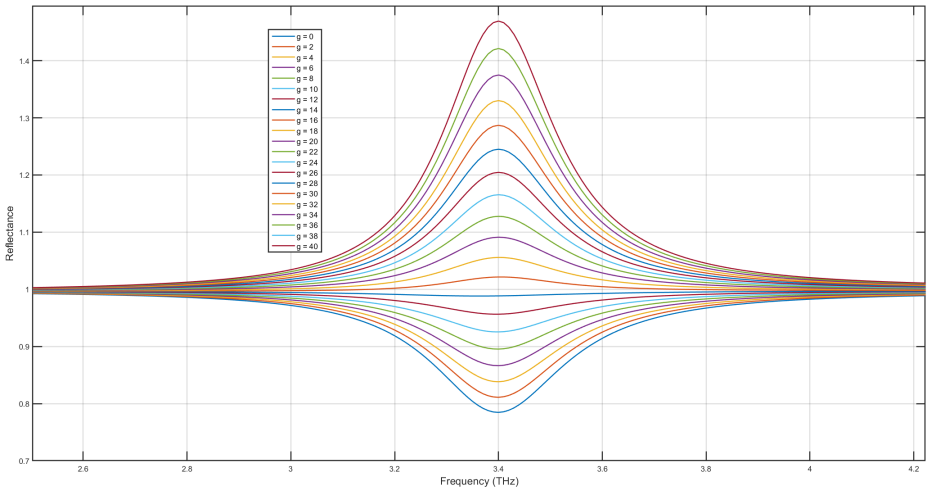

Figure 2.7: Reflectance of DW100 patch metasurface ($\Lambda = 50\,\mu$m) saturable absorber versus gain, assuming $\tau_{||,GaAs} = 0.3$ ps. Inset: The minimum reflectance of DW100 patch metasurface ($\Lambda = 50\,\mu$m) saturable absorber versus gain, showing a $g_{tr} = 14\,\text{cm}^{-1}$.

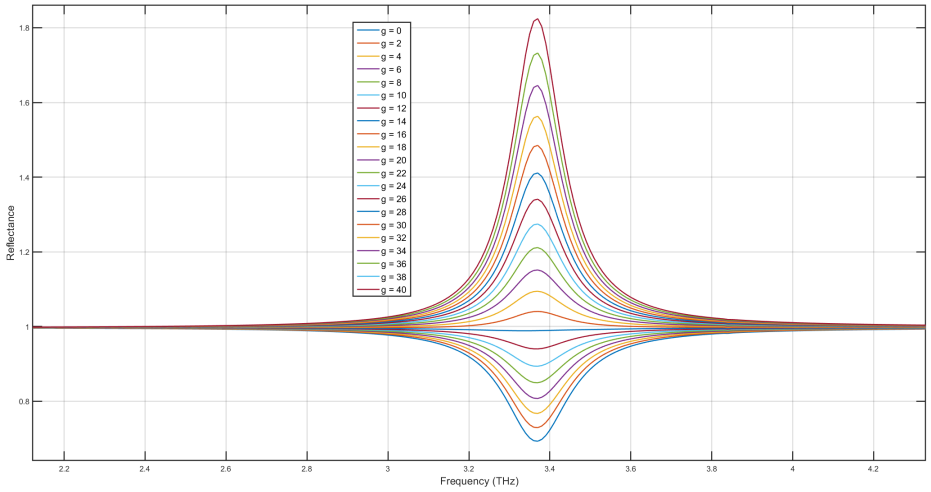

Figure 2.8: Reflectance of DW100 patch metasurface ($\Lambda = 60\,\mu$m) saturable absorber versus gain, assuming $\tau_{||,GaAs} = 0.3$ ps. Inset: The minimum reflectance of DW100 patch metasurface ($\Lambda = 60\,\mu$m) saturable absorber versus gain, showing a $g_{tr} = 14\,\text{cm}^{-1}$.

Metasurface Dispersion

Mode-locked lasers produce a train of pulses with a fixed phase relationship—hence the term "mode-locking." The coherence is limited by dispersion due to the finite bandwidth of

the gain medium, and phase accumulated from the mirrors each round trip. The SESAMs described in Chapter 1 utilize Bragg reflectors to define the phase of the saturable absorbers. Because the Bragg mirrors have a high refractive index contrast, the beam reflected from the mirrors can be designed to have 0 phase accumulation according to eq. 1.9. The QC metasurface saturable absorber, on the other hand, has a characteristic frequency-dependent phase and reflectance with contributions from the absorbing medium and the metasurface structure. Assuming a phase shift of π for the output coupler mirror of the QC-VECSEL cavity, the QC-VECSEL analogue for eq. 1.9 is:

$$2kL + \phi_{QC} + \phi_{SA} + \pi = 2\pi m, \tag{2.8}$$

where the subscripts QC and SA refer to the phase of the laser and the saturable absorber, respectively.

Metasurface QC-VECSELs in which each period consists of a single ridge waveguide feature reflectance spectra with a single resonance, generally controlled by the ridge width. The phase of the metasurface is a function of both period and ridge width. As was shown in Fig. 2.14, the resonances associated with single-ridge metasurfaces is generally sharp, and thus near resonance, these structures tend to lack regions of flat dispersion. However, the group delay dispersion (GDD) of the metasurface is typically much less than 1 ps^2.

In comparison, the addition of extra ridges of a different, but similar width to a period of the metasurface creates a close secondary resonance in the reflectance. This also manifests in the GDD as two peaks near resonance. The introduction of a second or third ridge within a period increases the dispersion relative to a single-ridge metasurface. The closer in width the two ridges are for a given period, the larger the magnitude of the GDD. To blunt the impact of the higher GDD in a passive metasurface, the ridge width and period can be engineered to decrease the GDD and shift the resonance such that the total dispersion near the lasing frequency is small. This also holds when increasing the number of patches in a

patch metasurface. It is difficult to say yet what amount of dispersion is tolerable until a saturable absorber-QC-VECSEL cavity is designed and tested.

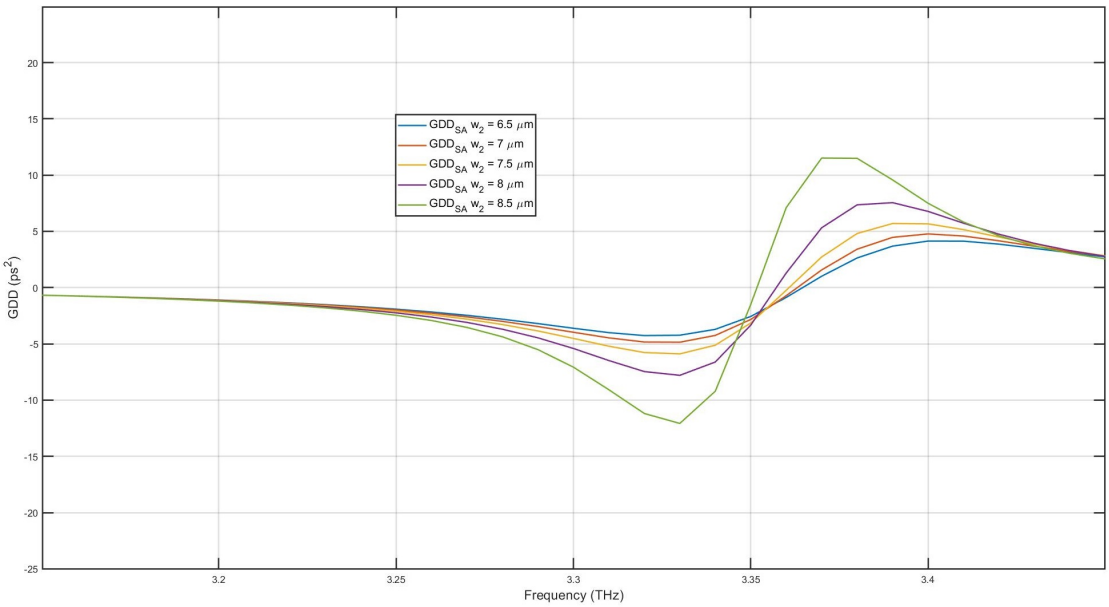

Figure 2.9: Group delay dispersion (GDD) of a double-ridge metasurface over various second-ridge widths, w_2, keeping $w_1 = 11.2\,\mu$m.

2.3 Reflectance Simulations for 3.4 THz QC-Metasurfaces

The initial ridge and patch metasurface saturable absorber designs were developed via simulations performed by my labmate Yu Wu in Ansys HFSS. In the COMSOL Multiphysics software, I calculated the ridge metasurface reflectance using a 2D simulation of a period of the saturable absorber. The geometry consists of a gold MM-ridge with what is effectively a GaAs active region. For the 250 nanometer gold layers, losses were represented using the Drude model, which describes the relationship between the frequency-dependent permittivity and free-carrier scattering losses. For gold, the Drude lifetime used throughout these simulations is 39 fs, but this may be greater than the Drude lifetime of carriers in gold at room temperature by $\approx 10 - 20$ fs [20], leading to an underestimation of the gold loss. That said, using the value of 39 fs does not change the relative change in reflectance with respect to incident intensity. The active region losses are calculated similarly, but only losses due to

intersubband absorption are incorporated. For the patch designs, only the patch is loaded with ISB gain, while the ridge connectors are assigned an uniform loss, $\epsilon_{r,GaAs} = 12.9$. Saturation of the ISB absorption transition is included phenomenologically using an effective permittivity. The populations of the two lowest subbands (n_{ISB}/L_{QW} in eq. 2.9) were used in determining an adjusted permittivity (ϵ_{ISB}) using the equation:

$$\epsilon_{ISB} = \epsilon_{GaAs} - \frac{n_{ISB} e^2 f_{12}}{\epsilon_0 m^* L_{QW} (\omega^2 - \omega_{ISB}^2 - i\frac{\omega}{\tau_{||}})} \times \frac{1}{1 + \frac{|E|^2}{E_s^2}}, \tag{2.9}$$

where f_{12} is the oscillator strength of the ISB transition, m^* is the effective mass in GaAs, ω_{ISB} is the center frequency of the ISB transition, $E_s^2 = 2\eta I_s$ is the square of the field and $\eta = \mu_0 c/n$, where c is the speed of light, and n is the refractive index of the material. The port of the model was loaded with input power, P_{in} (W/m) for the ridge metasurfaces, and P_{in} (W) for the patch designs,to determine the saturation intensities corresponding to dephasing times $\tau_{||}$ of 0.3 ps and 0.5 ps [15]. The COMSOL study swept P_{in} below and above estimated saturation to find the reflectance from 1 THz to 5 THz. Within COMSOL, the reflectance is calculated via eigenmode analysis at each port in the model. S-parameters are then calculated using methods similar to transmission line theory. Traditionally, the S matrix consists of the power reflection coefficient at each port of a transmission line, S_{ij}, where the second subscript denotes the excited port:

$$s = \frac{Z_L - Z_i^*}{Z_L + Z_i}. \tag{2.10}$$

In the equation above, Z_L represents the load impedance, and Z_i the internal impedance, both associated with an equivalent circuit [19]. In the case of optical analyses, it is more convenient to substitute electric fields with current and voltage. Thus, the reflectance at an excited port is given by

$$S_{ij} = \frac{\int_{port_i} (\boldsymbol{E_c} \cdot \boldsymbol{E_i^*}) dA_i}{\int_{port_i} (\boldsymbol{E_i} \cdot \boldsymbol{E_i^*}) dA_i}, \tag{2.11}$$

where $\boldsymbol{E_c}$ is the sum of the exciting and reflected fields at the port [4]. Reflectance calculations were made sweeping gain, input power, and angle. The results of these reflectance simulations were used to predict saturation intensity/field in each metasurface design, and show the impact of biasing on these values.

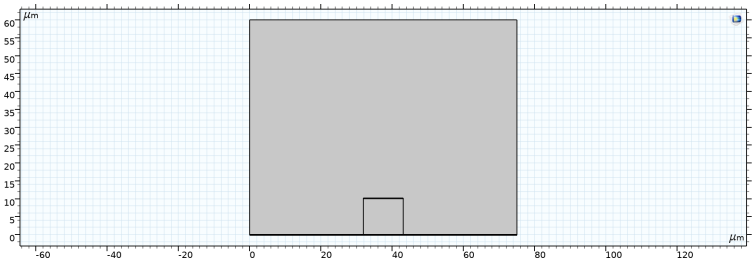

Figure 2.10: COMSOL model of DW100 ridge metasurface saturable absorber.

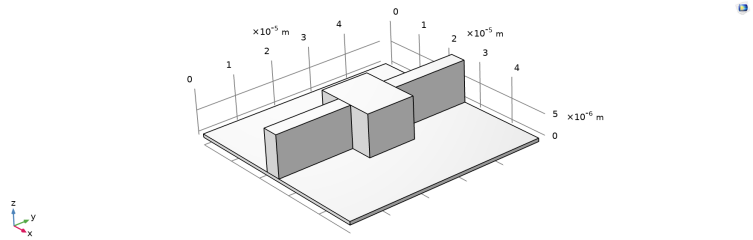

Figure 2.11: COMSOL model of DW100 patch metasurface saturable absorber.

Table 2.2: Dimensions of models used in COMSOL reflectance simulations.

Design	Ridge	Patch A	Patch B
Period	$\Lambda = 75$ μm	$\Lambda = 50\ \mu$m	$\Lambda = 60\ \mu$m
Dimensions	$w = 11.2$ μm	$w_1 \times w_2 = 15.2 \times 12 \mu\text{m}^2$	$w_1 \times w_2 = 15.2 \times 12 \mu\text{m}^2$

Table 2.3: Material parameters used in COMSOL reflectance simulations.

h_{active}	$10\,\mu$m
$\epsilon_{r,GaAs}$	12.9
m^*_{GaAs}	0.067
h_{Au}	250 nm
τ_{Au}	39×10^{-15} s [20]
n_{Au}	$5.9 \times 10^{28}\text{m}^{-3}$
$\omega_{p,Au}$	$1.37 \times 10^{16}\text{s}^{-1}$
$\omega_{p,GaAs}$	$1.54 \times 10^{13}\text{s}^{-1}$
σ_{GaAs}	$1.1426 \times 10^{-17}\text{m}^{-2}$
T	293 K

2.4 Nonlinear Modeling of Saturable Absorber Metasurfaces

The nonlinear behavior of the saturable absorber metasurfaces is characterized by the saturation intensity, I_{sat}, the saturation fluence, E_{sat}, and the saturable and nonsaturable losses.

In COMSOL, solutions to the wave equation in a 2D cross section of a single period of the ridge SA metasurface are used to solve for the frequency-dependent reflectance S_{11} at Port 1 (see Figure). An analytic value for the saturation intensity can be determined by repeating the simulation with added gain, and fitting the reflectance at resonance to the equation:

$$R = e^{\xi(g-g_{tr})} = e^{-\xi\alpha}. \tag{2.12}$$

Here, $\xi(\nu)$ is a factor that serves as an effective interaction length containing information on coupling between the gain medium and incident radiation. This will be used in the expression for the analytic saturation intensity. The derivation for this expression is similar to that of the saturation intensity of a two-level homogeneously-broadened medium. The

rate equations of such a system are:

$$\frac{dN_1}{dt} = \frac{N_2}{\tau_{21}} + \frac{\sigma(\nu)I_\nu}{h\nu}[N_2 - N_1] \tag{2.13}$$

and

$$\frac{dN_2}{dt} = -\frac{N_2}{\tau_2} - \frac{\sigma(\nu)I_\nu}{h\nu}[N_2 - N_1]. \tag{2.14}$$

In this equation, $N_{1,2}$ are the populations of the upper and lower lasing states, σ is the absorption cross section of the medium, and τ_{21}, τ_1 are the $|2> \rightarrow |1>$ transition time and the lower state lifetime, respectively.

Solving for $\frac{N_2}{N_1}$ yields

$$\frac{N_2}{N_1} = \frac{\frac{\sigma\tau_2 I_\nu}{h\nu}}{1 + \frac{\sigma\tau_2 I_\nu}{h\nu}} = \frac{I/I_s}{1 + I/I_s} \tag{2.15}$$

.

For a metasurface, the second term on the right hand side of $\frac{dN_1}{dt}$ and $\frac{dN_2}{dt}$ is replaced by the intensity-dependent term

$$\frac{I_\nu(1-R)}{h\nu h_r F},$$

representing the fraction of incident intensity absorbed by the metasurface. This term contains several factors unique to the metasurface under investigation: h_r is the height of the ridges that make up the reflectarray, and $F = \frac{w_{ridge}}{\Lambda}$, is the fill factor, the fraction of the width of the metasurface loaded with active material. To solve for the saturation intensity, R is expanded to first order in terms of the absorption cross section and population difference:

$$R = e^{\xi\alpha} = e^{-\xi\sigma(N_1 - N_2)} e^{-\xi\alpha_{ns}} \approx 1 - \xi\sigma(N_1 - N_2). \tag{2.16}$$

This means that the intensity absorbed by the metasurface is:

$$\frac{I_\nu(1-R)}{h\nu h_r F} = \frac{\xi\sigma}{h_r F h\nu} I_\nu(N_1 - N_2). \tag{2.17}$$

On inspection, this term increases when the effective interaction length ξ is a greater fraction of the height of the ridges, h_r, and also when the fill factor is decreased.

Applying this change to the rate equation above, the steady-state solution is determined by setting $\frac{dN_2}{dt} = \frac{dN_1}{dt} = 0$:

$$N_2[\frac{1}{\tau_2} + \frac{\xi\sigma}{h_r F h\nu} I] = \frac{\xi\sigma}{h_r F h\nu} I N_1 \tag{2.18}$$

Through some algebra,

$$\frac{N_2}{N_1} = \frac{\frac{\xi\sigma\tau_2}{h_r F h\nu} I}{1 + \frac{\xi\sigma\tau_2}{h_r F h\nu} I} = \frac{I/I_s}{1 + I/I_s} \tag{2.19}$$

Here, the term

$$(\frac{\xi\sigma(\nu)\tau_2}{h_r F h\nu})^{-1} \tag{2.20}$$

is defined as the saturation intensity, I_s.

Decreasing the fill factor or increasing ξ increases the intensity absorbed by the metasurface, which will result in lower saturation intensities. ξ is a value related to the quality factor of the metasurface. Higher ξ implies greater coupling efficiency between the metasurface active region and incident radiation [36]. Both decreasing the fill factor and increasing ξ are possible by increasing the metasurface period to an extent. The metasurface dimensions can be tuned to reduce the saturation intensity by two orders of magnitude relative to a slab of absorbing material. For this reason, the large period (75 μm) single-ridge saturable absorber metasurface and two patch designs simulated in the prior sections were considered.

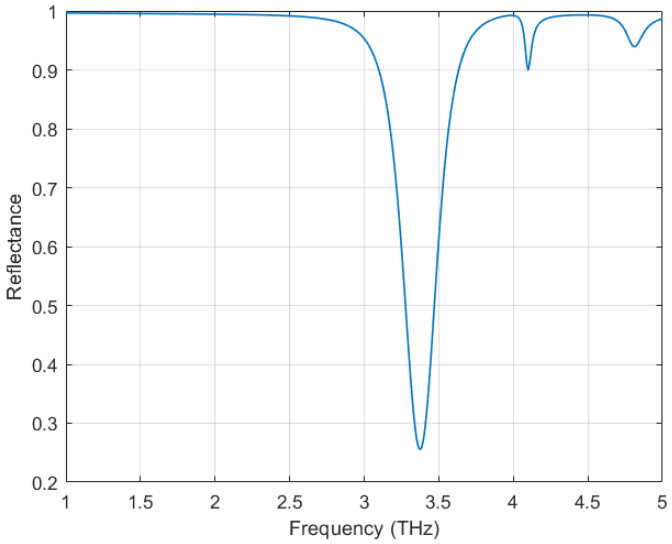

Figure 2.12: Reflectance of metasurface with ridge width 11.2 μm and period $\Lambda = 75$ μm. The metal is simulated with Drude loss, and the semiconductor has relative permittivity $\epsilon_{r,GaAs} = 12.9$. The minimum reflectance of 0.256 occurs at 3.7 THz.

The reflectance values plotted in Fig. 2.12 can provide insight on the validity of the ISB loss modeled in the prior chapter. The minimum reflectance in Fig. 2.12 is roughly 0.25. This can be compared to the reflectance due to the absorption in the DW100 material through $R = e^{-\xi\sigma(N_1-N_2)}e^{-\xi\alpha_{ns}}$. Substituting α from Fig. 2.5 into $R = e^{-\xi\alpha}$, something like an "upper limit" to the reflectance can be described. This would only evaluate the contribution of the ISB material on the reflectance, and disregard the other material losses and scattering influencing the results of the COMSOL simulation results.

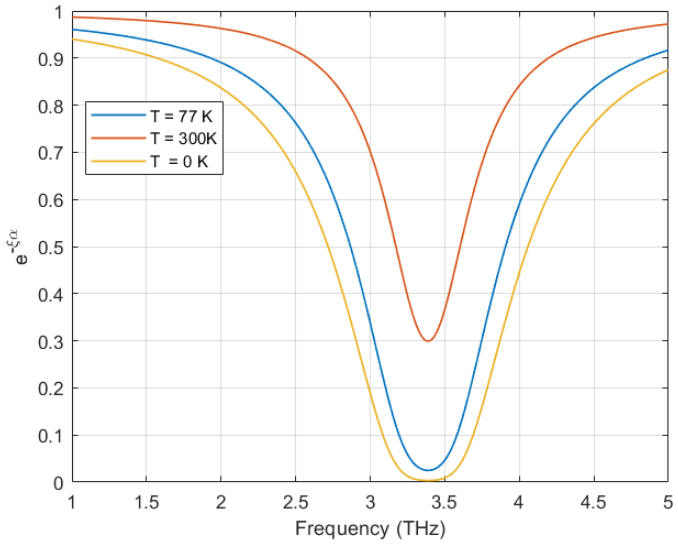

Figure 2.13: Reflectance of DW100 ridge metasurface saturable absorber as calculated using $\alpha_{300\,\mathrm{K}}$, $\alpha_{77\,\mathrm{K}}$, and $\alpha_{0\,\mathrm{K}}$.

Fig. 2.13 plots this "upper limit" using the equilibrium loss plotted in Fig. 2.5. The minimum reflectance at 3.9 THz is roughly 0.299, which agrees well with the COMSOL-derived minimum of 0.256 at 3.37. The fully relaxed absorption plotted in Fig. 2.5 similarly produces an estimated "lower limit" of reflectance, but for the given parameters, the reflectance approaches 0 at resonance, as this approximation is most accurate for lower α. A more robust calculation of subband populations and the inclusions of other material losses would improve the accuracy of this simulation.

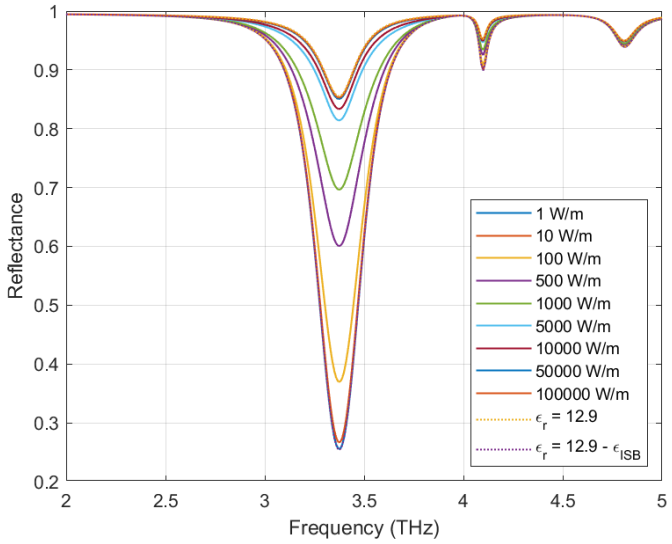

Figure 2.14: Reflectance of DW100 ridge metasurface saturable absorber versus input power assuming $\tau_{||,GaAs} = 0.3$ ps.

The single ridge SAMS featured a ridge width of 11.2 µm and a period of 75 µm. These reflectances were also calculated for a slightly longer dephasing time, 0.5 ps, but the curves differed only slightly. The previous figure shows the reflectance of the ridge SAMS over P_{in}, and Figs. 2.16a, 2.16b show the same for Patch A and Patch B, respectively. The saturation of the reflectance is clearly visible when plotted alongside the reflectance with a uniform permittivity $\epsilon_{GaAs} = 12.9$, which serves as the upper limit of reflectance, and alongside the lower limit, in which the saturable loss ϵ_{ISB} sees $\frac{|E^2|}{E_s^2} \approx 0$. The minimum reflectance is plotted as a function of input intensity in the following figures. To derive a saturation intensity from these figures, the axes were interpolated to find the intensity which corresponded to a reflectance closest to half the modulation depth, ΔR, which is the difference between the linear reflectance and the fully saturated reflectance. This value is 559 W/cm^2 in the case of $\tau_{||,GaAs} = 3$ps and 525 W/cm^2 in the case of $\tau_{||,GaAs} = 5$ps. These are both on the same order of magnitude of the analytic saturation intensity given in Table 2.5, and the estimate can be further refined by adding more points to the data in Figures 2.15a and 2.15b.

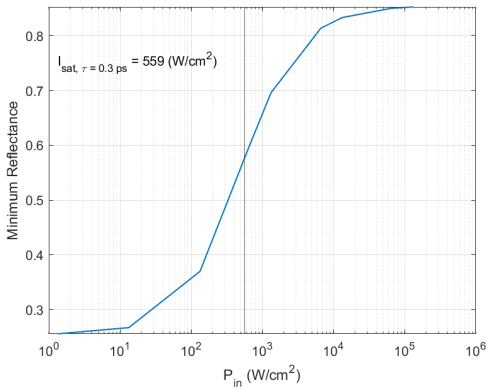

(a) $\tau_{||,GaAs} = 0.3$ ps.

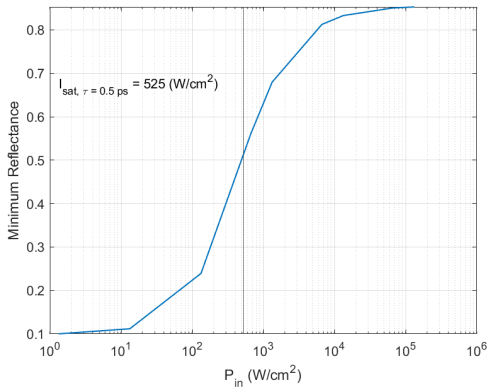

(b) $\tau_{||,GaAs} = 0.5$ ps.

Figure 2.15: Minimum reflectance of DW100 ridge metasurface saturable absorber versus incident intensity, assuming (a) $\tau_{||,GaAs} = 0.3$ ps and (b) $\tau_{||,GaAs} = 0.5$ ps.

Two saturable absorber patch metasurfaces were also simulated, Patch A, with period $\Lambda = 50$ µm and Patch B with $\Lambda = 60$ µm:

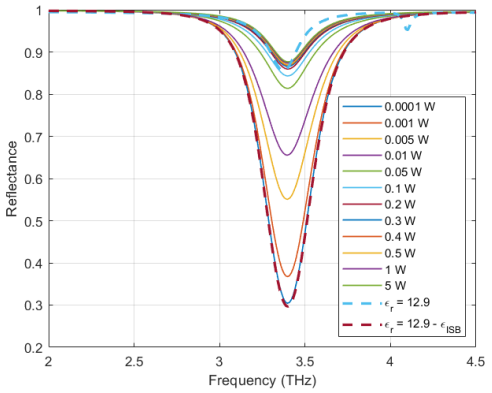

(a) $\Lambda = 50$ µm, $\tau_{||,GaAs} = 0.3$ ps.

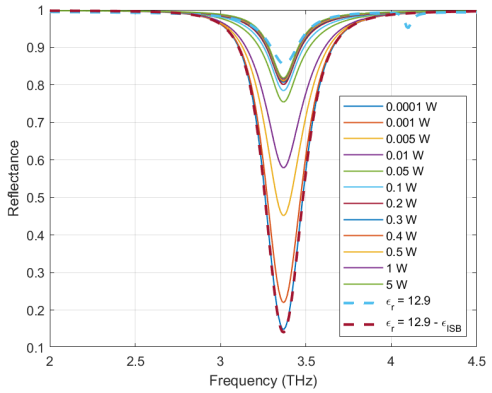

(b) $\Lambda = 60$ µm, $\tau_{||,GaAs} = 0.3$ ps.

Figure 2.16: Reflectance of DW100 patch metasurface for a), $\Lambda = 50$ µm and b) $\Lambda = 60$ µm saturable absorber over various input power [W], assuming $\tau_{||,GaAs} = 0.3$ ps.

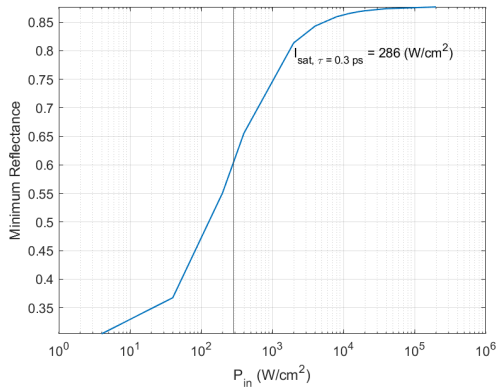

(a) $\Lambda = 50$ µm, $\tau_{||,GaAs} = 0.3$ ps.

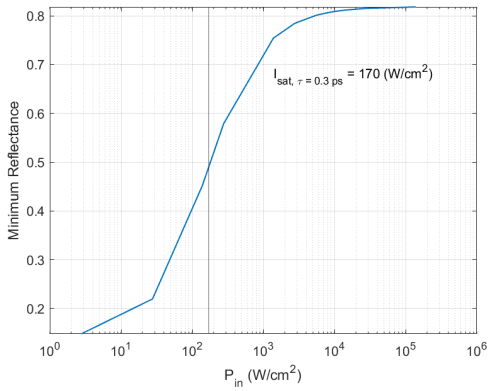

(b) $\Lambda = 60$ µm, $\tau_{||,GaAs} = 0.3$ ps.

Figure 2.17: Minimum reflectance of DW100 patch metasurface saturable absorber a) $\Lambda = 50$ µm, and b) $\Lambda = 60$ µm versus intensity, assuming $\tau_{||,GaAs} = 0.3$ ps.

Both the ridge and patch reflectance at resonance over incident powers matches closely with the theoretical relationship for SESAMs, with metal losses contributing mostly to the loss at low incident powers. The interpolated patch reflectance further supports the theory that reducing fill factor lowers the saturation intensity.

Following Keller [16], the slopes of these reflectance versus input intensity curves provides information on the time needed to produce mode-locked pulses, and whether or not Q-switching instabilities occur. The build-up time is given by:

$$T_{build-up} \propto \frac{1}{\frac{dR}{dI}_{I\approx 0} I}. \tag{2.21}$$

The faster the reflectivity changes with intensity (the larger the slope), the shorter the build-up time required to reach mode locking. Real device characterization is still needed to determine whether or not mode locking could self-start in a QC-VECSEL cavity with a metasurface saturable absorber; if it is possible, lower saturation intensities would enable short build-up times.

To prevent Q-switched mode-locking behavior, the intracavity pulse energy, E_p, has the following constraint:

$$E_p^2 > E_{sat,L} E_{sat,A} \Delta R, \tag{2.22}$$

where $\Delta R = R_{ns} - R_{lin}$. The modulation depth calculated via COMSOL for each saturable absorber metasurface design are given in Table 2.4, and Fig. 2.18 provides an illustration of the variables used to compute E_p^2. It is apparent that the patch metasurfaces require a lower intracavity pulse energy to prevent mode-locking instabilities. This is owed to their inherently lower saturation fluences caused by smaller fill factors. These fluence estimates can be validated by characterizing these devices with a high-power, pulsed laser. Table 2.5 shows the analytic saturation intensities of the three metasurface designs. Based on the analytic saturation intensities, a 3.4 THz beam with radius 0.5 mm would fully saturate the ridge metasurface at a power of roughly 2.6 W. This clearly scales with decreased fill factor, pushing the power required to mode lock a QC-VECSEL down to 620 mW for Patch B.

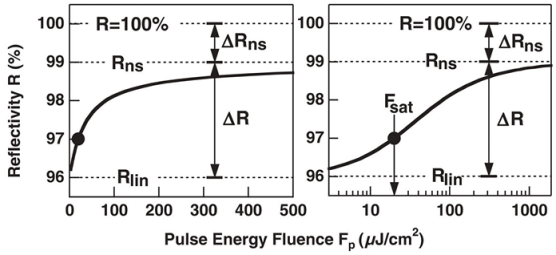

Figure 2.18: Theoretical reflectance over incident pulse fluence, from [8].

Table 2.4: Estimated Saturation Fluence for Saturable Absorber Designs ($\tau_{||,GaAs} = 0.3$ ps). The subscripts i, a denote the interpolated and analytic solutions, respectively.

Design	Ridge	Patch A	Patch B
ΔR	0.597	0.5724	0.6701
$E_{p,a}$ (V/m)	$> \sqrt{1.18 \times 10^4 E_{sat,L}}$	$> \sqrt{8.5 \times 10^3 E_{sat,L}}$	$> \sqrt{6.5 \times 10^3 E_{sat,L}}$
$E_{p,i}$ (V/m)	$> \sqrt{2.57 \times 10^4 E_{sat,L}}$	$> \sqrt{1.84 \times 10^4 E_{sat,L}}$	$> \sqrt{1.42 \times 10^4 E_{sat,L}}$

Angled simulations were also performed on the patch metasurface designs, but these showed that the reflectance varied too greatly for even small changes in angle to be useful in initial measurements.

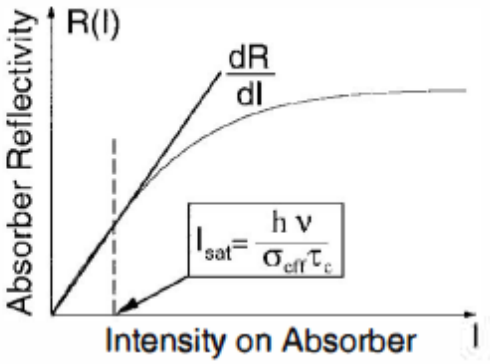

Figure 2.19: Theoretical reflectance over incident CW intensity.

Table 2.5: Analytic (a) and interpolated (i) saturation parameters for DW100 samples, assuming $\tau_{||,GaAs} = 3$ ps.

Design	Ridge	Patch A	Patch B
ξ (cm)	0.01772	0.01533	0.02498
F (%)	14.93	7.296	5.07
$I_{sat,a}$ (W/cm^2)	330	187	80
$I_{sat,i}$ (W/cm^2)	559	286	170
$R_{ns,i}$	0.853	0.877	0.818

Chapter 3

Experimental Design and Transmission Measurements

3.1 Mid-IR Single-Bounce Transmission

In this chapter, FTIR spectroscopy is used to characterize the reflectance of mid-IR and THz absorber samples. The 10 μm SW66 absorber designed had a less complicated characterization set up than the DW100 metasurfaces to be discussed later in the chapter. The SW66 wafer was not patterned into metasurfaces; instead, the material absorbance was measured inside the FTIR after being cleaved and polished. The SW66 wafer was cleaved into roughly roughly 2 mm wide pieces. The pieces were polished at 45 degree angles using a Logitech PM5 polisher and slurry using a premade chuck. According to multi-bounce calculations following Liu and Capasso [21], this combination of polishing angle and dimensions would allow us to take single-bounce transmission measurements within the sample compartment of an FTIR. A beam condenser accessory to the FTIR was used to take the transmission measurements.

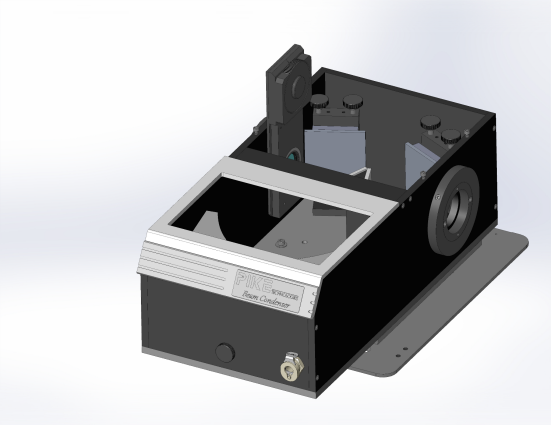

(a) Pike beam condenser, figure from [3].

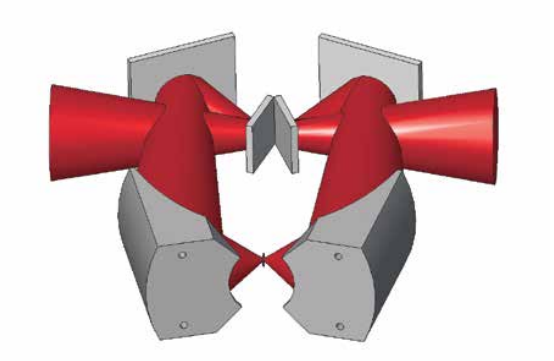

(b) Optical diagram of beam condensing, from [3]

.

The sample is clamped down by the screws in the metal sample holder and rests on either the adjustable stage or the stable mount. The mount goes between the two curved mirrors. There are pegs in the beam condenser that slot into holes on the mount. There is also a screw on both mounts that lines up with a hole near the middle of the beam condenser to keep the mount steady. The beam condenser is inserted into the sample compartment with the detector facing the thicker viewport. A polarizer was inserted into the space between the wall of the beam condenser and the mirror snugly. As the SW66 growth stack was designed for absorption near 10 microns, a mercury cadmium telluride (MCT) detector was used in conjunction with the FTIR. A separate sample holder from the beam condenser kit and the translation stage were used to to align the sample. Making slight adjustments to the translation stage maximized power at the detector. A polarizer was clamped to the window of the beam condenser After closing the sample holder of the FTIR, it was left to purge before measuring transmittance.

Figure 3.2: Photograph of FTIR sample compartment with beam condenser and polished SW66 sample.

The relative transmission measured using the FTIR was as low as 6 percent at 98 meV ($\sim$ 12.65 µm). This sharp dip is most likely due to atmospheric absorption caused by an imperfect purge. That said, the presence of the dip near the expected resonance was consistent between measurements; with the only the magnitude varying with polarization. Using the measured data, absorbance was calculated assuming $Abs = 2 - log_{10}(T)$. The equation for transmission through a polished wedge of MQW material was used to solve for α_{3D} by dividing α_{2D} by 1 cm (near the dimension of the longest edge of the piece). This was fit to Lorentzian and Gaussian curves to produce values of 259cm^{-1} and 246cm^{-1} near 12.2 µm, respectively. This is greater than the absorption coefficient calculated in MATLAB,

which does not consider losses from the metal or other sources of loss within the path of the FTIR.

While using the glow bar source inside the FTIR allowed me to derive an absorption coefficient for a mid-IR sample, the THz output power available using the internal FTIR source would not be suitable for a similar experiment on the DW100 samples. To remedy this, an external transmission measurement for the SW66 samples was designed:

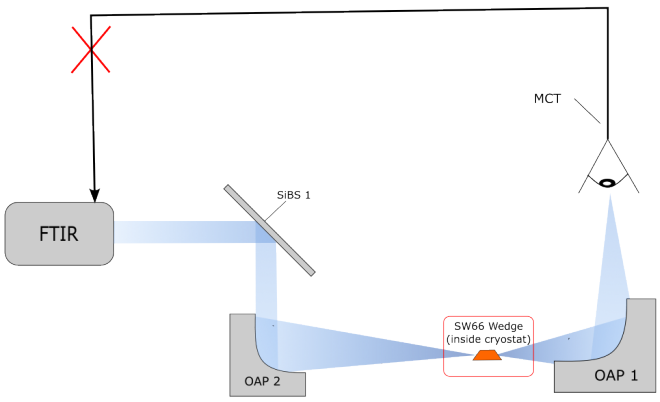

Figure 3.3: Proposed external transmission measurement design for SW66 samples.

The source in the design depicted in Fig. 3.3 was again the glow bar, but a beamsplitter was used to direct the radiation into a cryostat housing a SW66 wedge. The beam would bounce once in the wedge, and travel through the rear window of the cryostat before being focused onto a cooled MCT detector. The He-Ne beam within the FTIR was used to align the beamsplitter and OAPs onto the detector window. The detector was connected to a preamplifier linked to the FTIR, but ultimately the electronics were incompatible. A similar design was conceived for the DW100 sample, in which a pyroelectric detector would be connected to the FTIR, but a similar issue occurred.

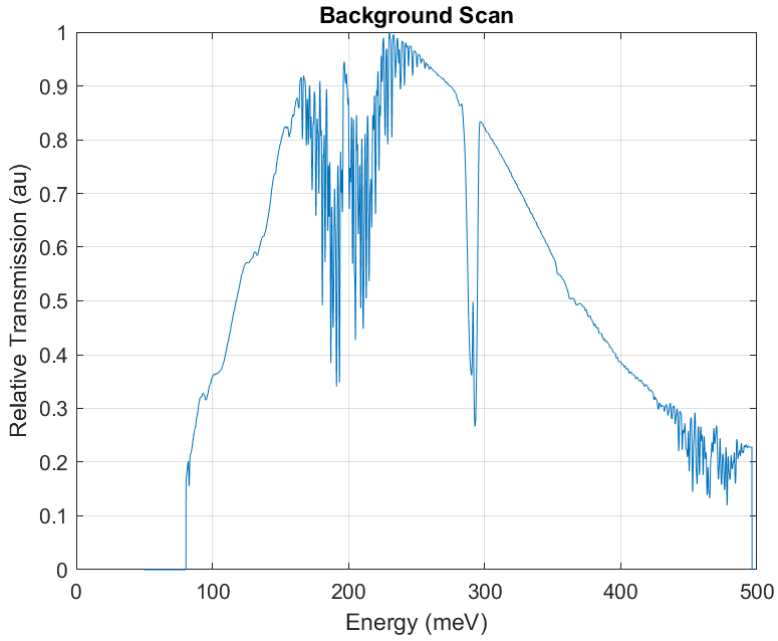

Figure 3.4: The FTIR background spectra used to measure relative transmission.

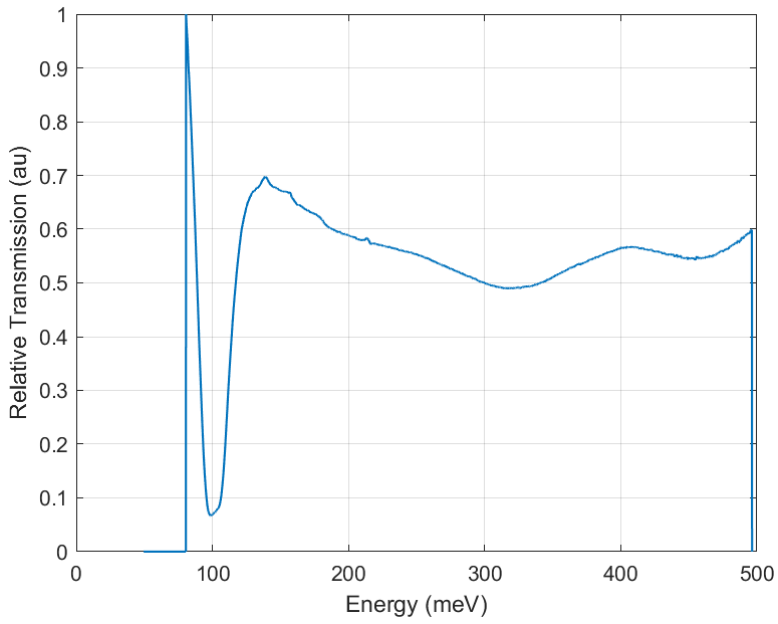

Figure 3.5: Relative transmission of polished SW66 piece ($l = \ 2mm$).

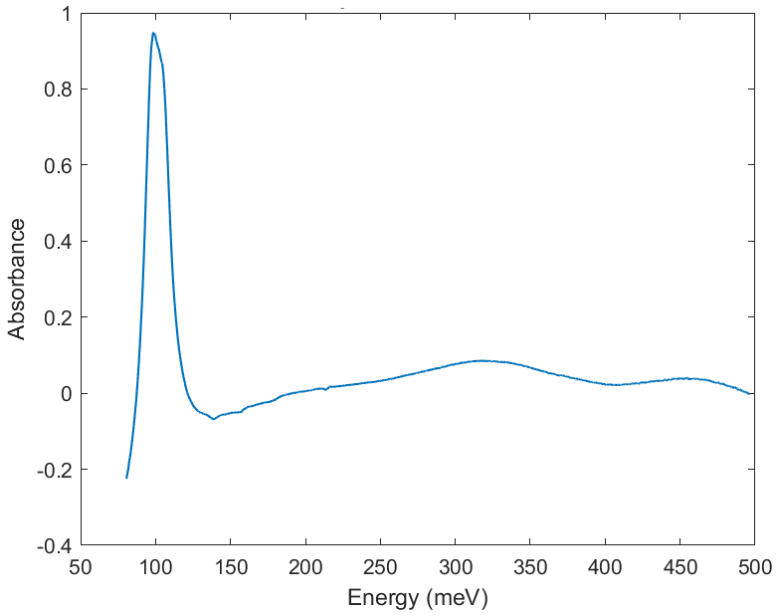

Figure 3.6: The absorbance of the 2 mm SW66 wedge from experimental data.

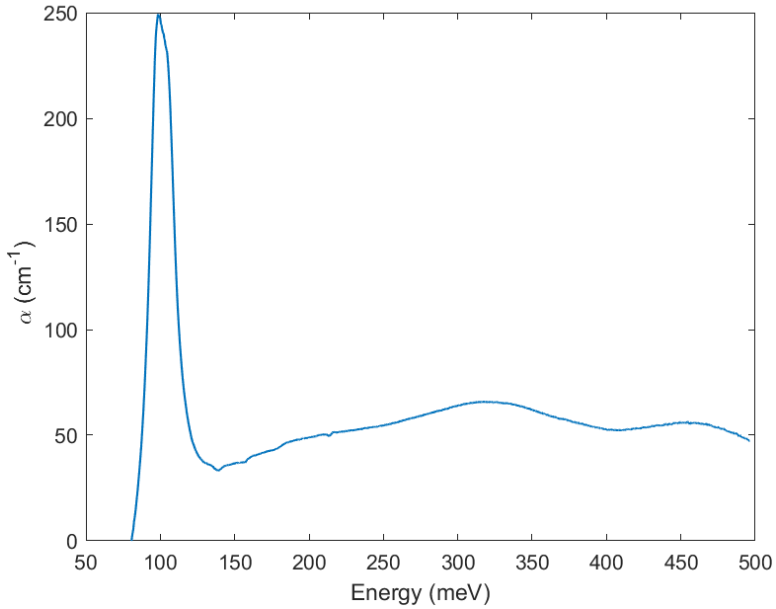

Figure 3.7: The absorption coefficient of the 2 mm SW66 wedge derived from experimental data.

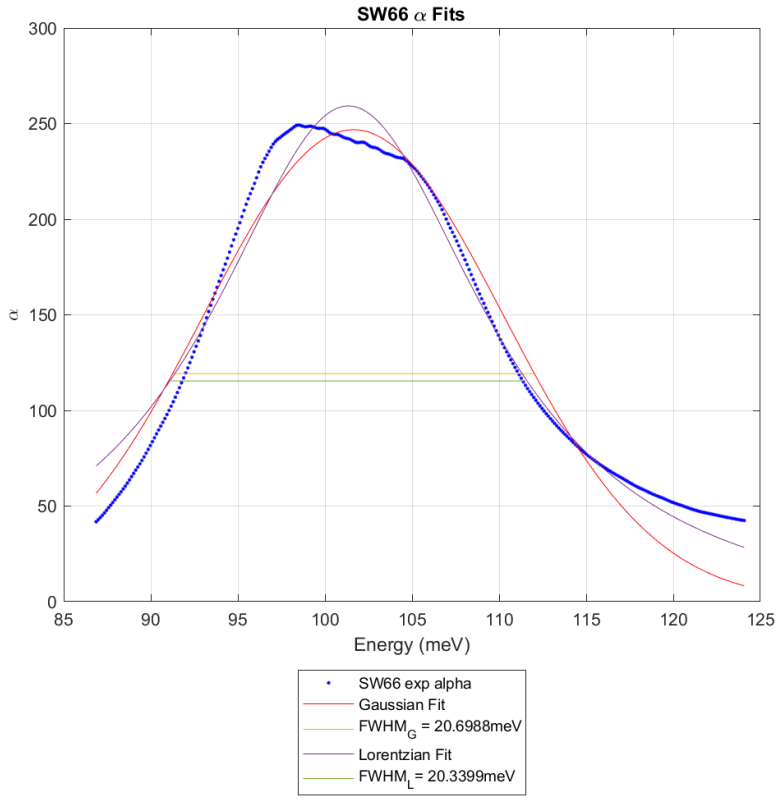

Figure 3.8: The absorption coefficient of the 2 mm SW66 wedge derived from experimental data.

3.2 Source Characterization

The simulations discussed in the prior sections provided estimates of the saturable and nonsaturable losses of the metasurface saturable absorber samples. This chapter will detail the experimental design used to characterize the saturable absorbers' reflectance. Traditional reflection-mode spectroscopy using a bolometer was unavailable because of a nationwide liquid helium shortage. To circumvent this, reflection-mode transmission measurements were taken using QC-VECSELs as an external source for the FTIR. The larger output power from the QC-VECSELs ($> mW$) allows the use of room-temperature pyroelectric detectors instead of a liquid-helium-cooled bolometer.

The ideal source for characterizing the saturable absorber metasurfaces discussed in previous sections is a high-power device that lases near 3.4 THz and is tunable at least over the

expected absorption feature of the saturable absorber metasurface. Several prefabricated devices were tested, most consisted of a 4 well active region with a $2 \rightarrow 1$ transition energy of ≈ 14 meV at design bias. Large area metasurface ($D_{bias} \geq 1$mm) QC-VECSELs were prioritized.

3.2.1 Current-Voltage-Power Measurements

The source QC-VECSEL, U-3.4-B1, was a TM01, single-ridge metasurface that lased between 3.15 THz and roughly 3.34 THz, roughly 60 GHz off-resonance of the 3.4 THz saturable absorber. The laser had a bias diameter of $D_{bias} = 1$ mm.

The QC-VECSELs tested were prepared as follows: A piezoelectric stage, a nanopositioner from Attocube, was screwed onto the cold plate of a cryostat (IRLabs dewar). The QCL was mounted onto a copper heat sink with screws; generally the chip carrier was backed with indium foil to improve heat sinking. An SMA adapter is also screwed to the heat sink and soldered to the gold pad on the chip carrier. The QC-VECSEL on the heat sink is secured behind the nanopositioner. Alignment is performed using a He-Ne beam. As the beam shines onto the QC-metasurface, the reflection forms a diffraction grating made visible by a sheet. The zeroth order mode is centered by adjusting the dewar. Then, the output coupler, having been screwed onto a separate copper mount, is secured onto the nanopositioner. As the He-Ne beam shines through the output coupler onto the QC-metasurface, the reflection forms a separate grating that can be centered on the same spot as that formed by the QC-metasurface. Small screws on the output coupler mount allow for slight adjustments to tilt. An SMA cable is screwed to the adapter soldered to the device. Before closing the dewar, the piezoelectric stage is adjusted to minimize the external cavity length. After, the dewar is connected to a vacuum pump and cooled to liquid nitrogen temperature (77K).

The devices were biased as follows: The device is biased using a pulse generator. QC-VECSELs tested were usually driven at 0.5% (10 kHz frequency) to 1% (20 kHz frequency) duty cycles with a pulse width of 500 ns. The input voltage and current are sent through

boxcar averagers (one to probe voltage and the other current) via BNC connectors from the current sensor. The output of each boxcar is connected to a digital multimeter used to provide measurement data in LabVIEW. The power emitted from the THz QC-VECSEL is measured using a pyroelectric detector (Gentec) whose output is connected to a lock-in amplifier (LIA). Because the pyroelectric detector is unable to resolve changes in radiated power due to the kHz frequency pulses driving the laser, the pulser must be gated by a frequency generator, also used as a reference for the LIA. For power measurements, a gate frequency f_{gate} of 20 Hz was used. LabVIEW was used to control each component via GPIB connections to each component.

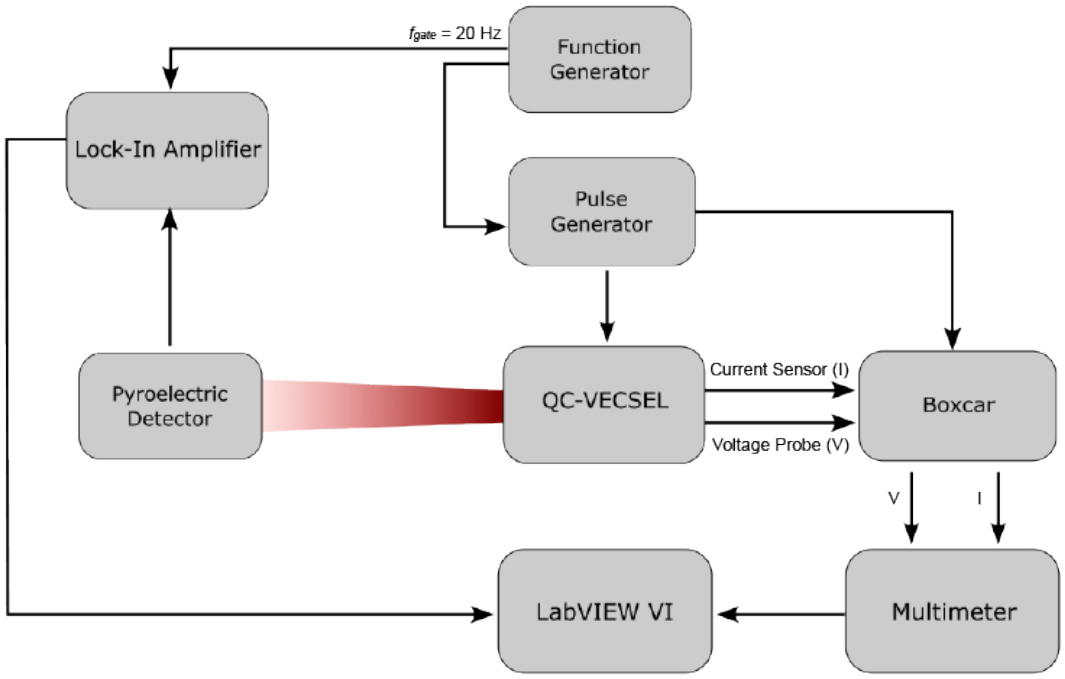

Figure 3.9: Current-voltage measurement setup.

3.2.2 Spectral Measurements

Once the current-voltage-power data was collected, the function generator is disconnected and an OAP mirror was used to reflect light into the Fourier Transform Infrared Spectrometer (FTIR). The terahertz radiation passes through an interferometer and is detected by a

deuterated triglycine sulfate (DTGS) detector inside the FTIR. The OAP position and dewar height are adjusted to maximize the signal on the detector, as seen through the interface of the FTIR software OMNIC. An acrylic purge box is then placed over the optical path to remove traces of water vapor. The device is biased near max power and the piezoelectric stage is stepped such that the external cavity lengthens. After each step, another spectrum is acquired.

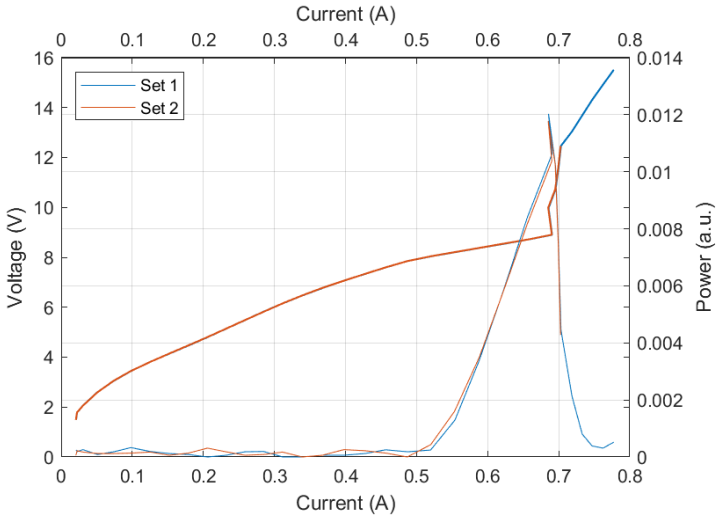

Figure 3.10: LIV for U-3.4-B1.

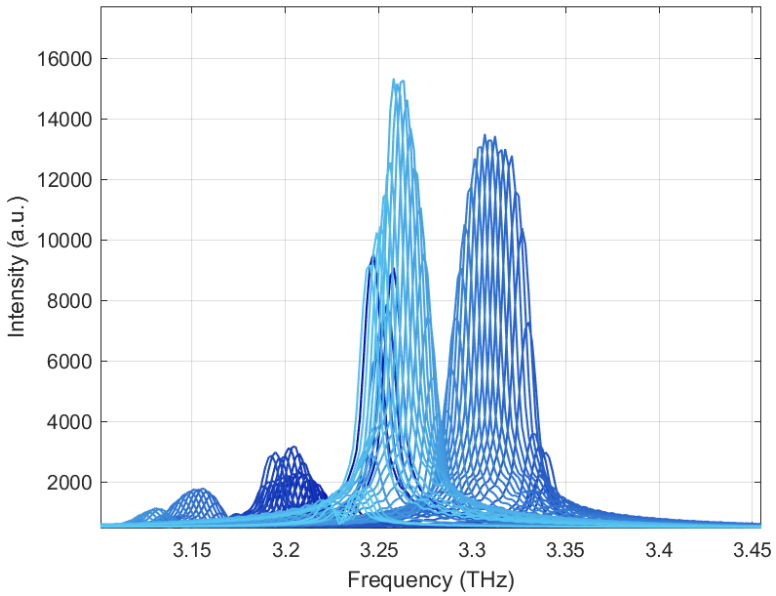

Figure 3.11: Spectra for U-3.4-B1

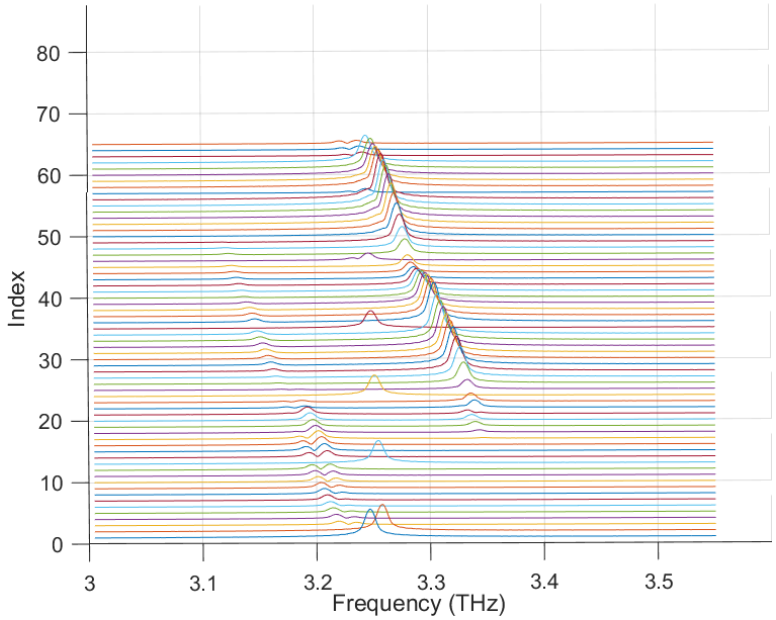

Figure 3.12: Spectra for U-3.4-B1

3.3 Reflection-Mode Transmission Measurements

3.3.1 Alignment Procedure

Because of the relatively long path length involved, alignment of the terahertz QC-VECSEL in these reflection-mode transmission measurements is a highly sensitive process. A helium-neon beam was used to align each optical element one at a time. Firstly, the QC-VECSEL was positioned. The terahertz beam reflected off the first OAP (OAP 1) onto a gold mirror, and from that gold mirror, into a terahertz camera. The angle and position of OAP 1 was adjusted to center the terahertz beam in the camera. The camera could then be moved towards and away the gold mirror to ensure the beam remained collimated at a 90 degree angle to OAP 1. The second OAP (OAP2) was positioned ≈ 18 in apart from OAP 1. A He-Ne laser was positioned where the QC-VECSEL sat, and adjusted to bounce off OAP 1 and OAP 2 onto a gold mirror (AUM1). The retro-reflected He-Ne beam could be steered by adjusting the angle of OAP2 to fall onto the aperture of the He-Ne, thereby assuring the incident path is identical to the reflected path. Next, the silicon beamsplitter (SiBS 1) is positioned between OAP 1 and OAP 2 with enough clearance to fit detectors or cameras. Replacing the He-Ne with the QC-VECSEL again, but leaving AUM1 at the focal point of OAP 2, another gold mirror, AUM2, was placed to the left of SiBS 1, near the window of the FTIR, and angled to reflect the terahertz beam onto the terahertz camera. The appearance of a centered, collimated beam at the terahertz camera confirms the position, height, and angle of SiBS 1 and of the QC-VECSEL. Upon removal of AUM2, the terahertz signal at the FTIR is strong enough to take transmission measurements.

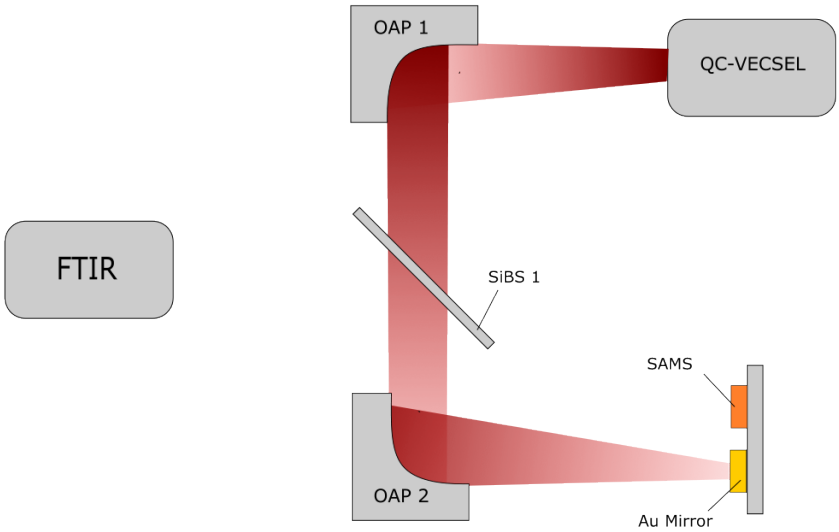

Figure 3.13: The incident optical path from the QC-VECSEL to the saturable absorber and reference mirror.

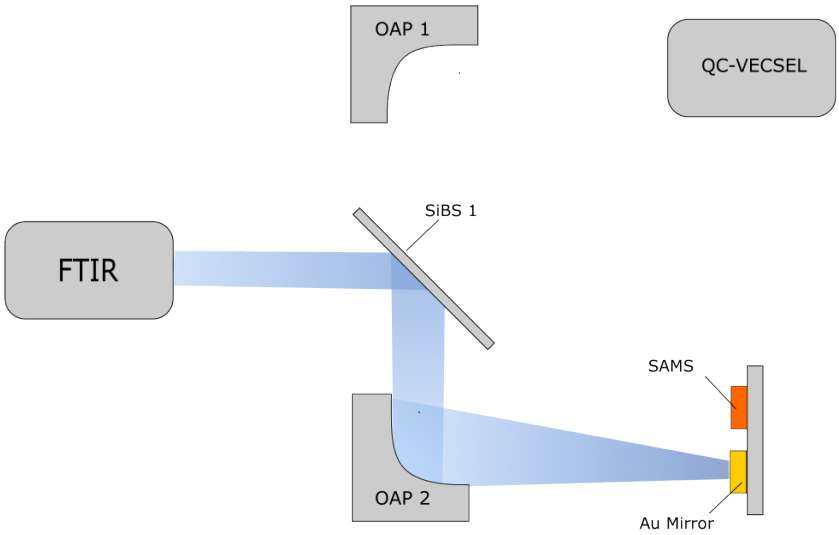

Figure 3.14: The optical path of the reflected QC-VECSEL beam.

3.3.2 Two-Detector Setup

To measure power directly rather than indirectly use the DGTS detector within the FTIR to compare reference and sample, a second silicon beamsplitter will be added (SiBS 2), such that light from BS1 moving toward the FTIR is partially redirected onto a pyroelectric detector using a lens. The partially reflected light that from the sample or reference will be guided into a second pyroelectric detector in a similar fashion.

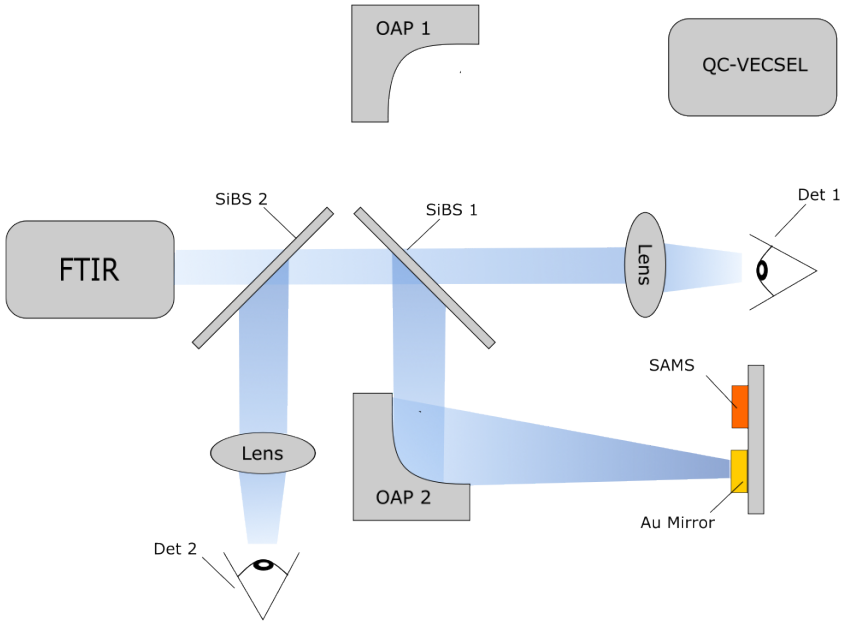

Figure 3.15: The proposed two detector setup allowing for direct power measurement.

3.3.3 Beamsplitter Characterization

To ensure that SiBS 1 would not overly-attenuate the signal reaching the FTIR, a high-power QC source was used to measure the reflectance of the beamsplitter. The reflectance of the beamsplitter was measured by placing it at a 45° angle so that the terahertz radiation was reflected into the FTIR. Like in the spectral measurements for the laser, a spectrum was acquired after each step of the piezoelectric stage holding the output coupler. After sweeping the full lasing spectrum of the source, the nanopositioner was stepped back to roughly its initial distance from the QC-metasurface. The spectral measurements were then repeated with a gold reference mirror. The intensity measured by the FTIR over each frequency for both the reference and the beamsplitter was plotted.

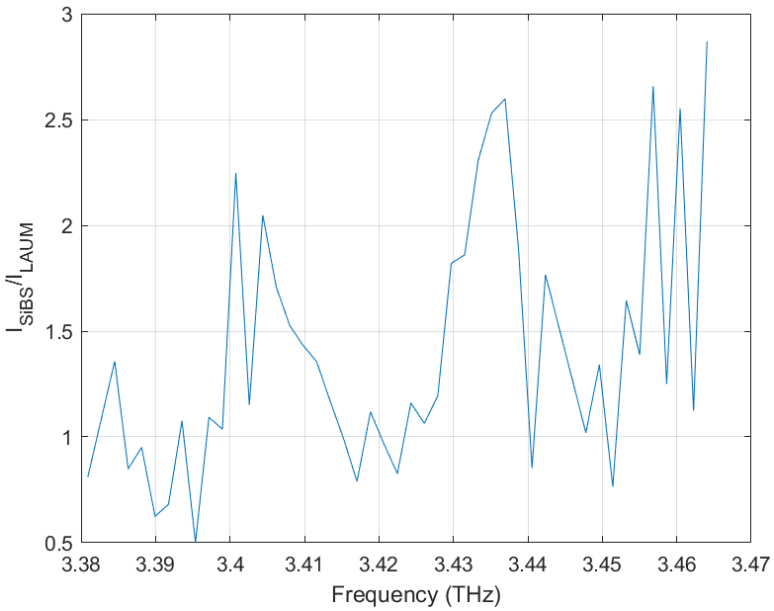

Figure 3.16: Reflectance of the Si beamsplitter at 45 ° measured with a high-power QC-VECSEL.

The ratio of these values I_{Mirror}/I_{Sample} represents the reflectance. Although the profile of the beamsplitter was thin, Fabry-Perot reflections likely contributed to the measurement results. The noise in the data also indicates poor signal at the detector in the FTIR, probably due to poor alignment. This was corrected by re-aligning the set up and taking a 100% scan

to measure the improved signal (results in the next section). The beamsplitter efficiency, η_{BS}, was calculated for s- and p-polarized light, following [13]. The efficiency oscillates over the lasing spectrum of U-3.4-B1 for both polarizations, with the s-polarized light experiencing $\eta_{BS} > 50\%$ for much of the lasing spectrum and p-polarized light near 30% efficiency. The polarization of the beam from the QC-VECSEL is determined by how the device is mounted; in future measurements, a waveplate or polarizer will be added to the set up to control the polarization of the beam.

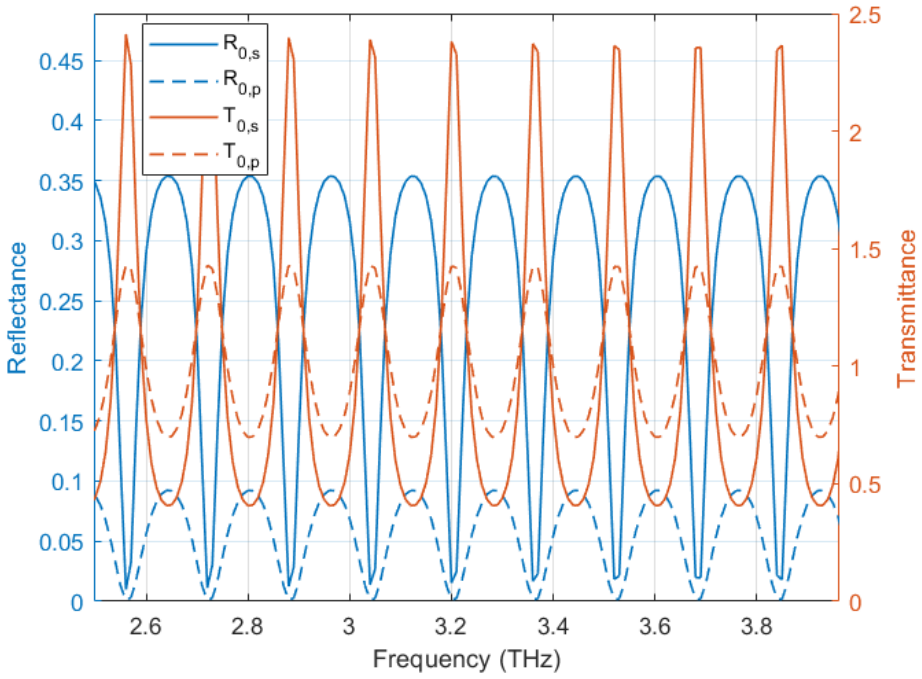

Figure 3.17: Calculated reflectance and transmittance of SiBS 1 at 45 °, assuming a width of 280 microns, for s- and p-polarized light following [13]. Fabry-Perot fringes are visible.

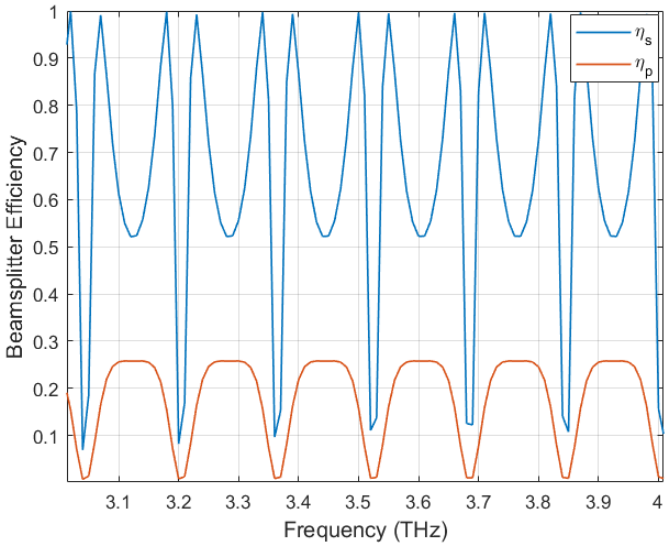

Figure 3.18: Beamsplitter efficiency of SiBS 1 for s-polarized and p-polarized light at an angle of 45° between 3 and 3.5 THz, assuming a width of 280 microns, following [13].

3.3.4 100% Scan

Before placing the saturable absorber sample in the position of AUM_2, the mirror was left in its position to perform a 100% scan using the FTIR. In this measurement, noise was characterized by measuring transmission as reflected from a large, flat mirror twice in a row across the lasing range of a tunable QC-source. Ideally, the ratio of the power received at the DGTS detector within the FTIR from both sweeps would be 1. Measuring the deviations from unity in the reflectance provides a sense of error in all measurements. The 100 % scan shows a $\approx \pm 4\%$ deviation from the expected reflectance of 1. In future measurements, I will use more scans to calculate a more accurate SNR, assuming $SNR = \mu/\sigma$, where μ is the mean of the spectra and σ is the standard deviation across scans.

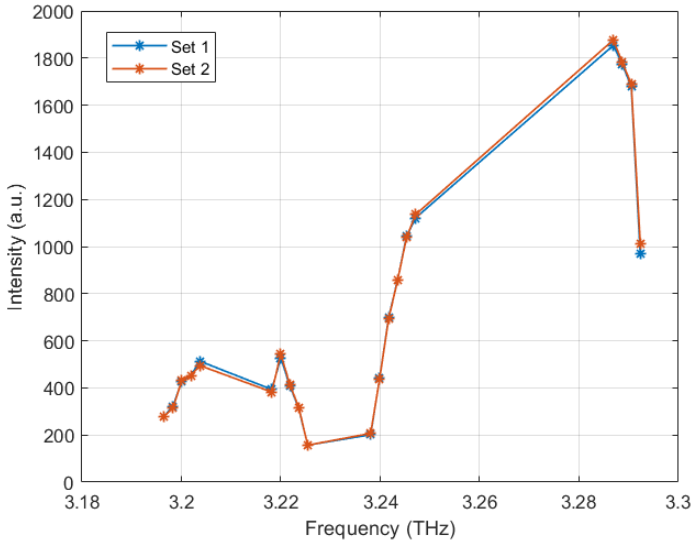

Figure 3.19: FTIR measurements of the reference mirror for the 100% scan..

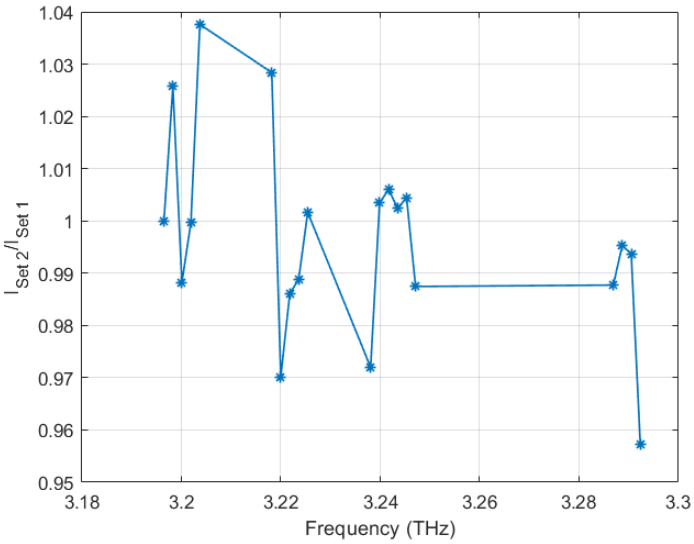

Figure 3.20: Reflectance of reference mirror.

3.3.5 Measuring Reflectance of Metasurface Saturable Absorber

The reflectance of the saturable absorber sample was measured the same way as the large, flat mirror in the 100% scan. The sample and reference mirror were clamped on a raised mount, on top of a translational stage. The stage was controlled using a stepper motor connected to a LabVIEW VI via USB. The VI automated the process of stepping the translational stage such that the reference mirror was in the optical path, recording the reflected background spectrum using the FTIR, stepping the stage such that the metasurface was in the optical path, and recording another spectrum before lengthening the QC-VECSEL cavity. The data acquired using U-3.4-B1 in the 100% scan data as well as that in Fig. 3.21b, was collected after optimizing the alignment procedure. This is evidenced by the more uniform spectra between the reference and the saturable absorber. The lasing spectrum of U-3.4-B1 did not cover the resonance dip of the saturable absorber, therefore it is difficult to gauge whether the reflectance decreases towards 3.4 THz. Due to a large atmospheric absorption dip near 3.23 THz, 6 data points near 3.23 THz were removed.

The U-3.4-B1 device was damaged after using a 14 A pulser with a poor pulse shape, and thus few rounds of measurements could be taken. The improved alignment procedure coupled with a source closer to the metasurface resonance will produce clearer data. New QC metasurfaces are currently being fabricated; these are designed to tune over at least 400 GHz and fully cover the expected resonance.

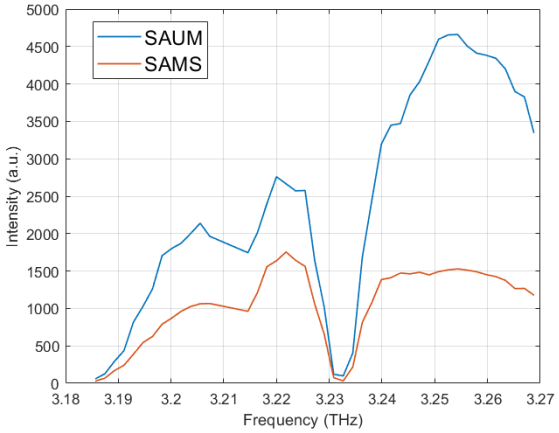

(a) Reflected FTIR spectra from reference and sample, using U-3.4-B1.

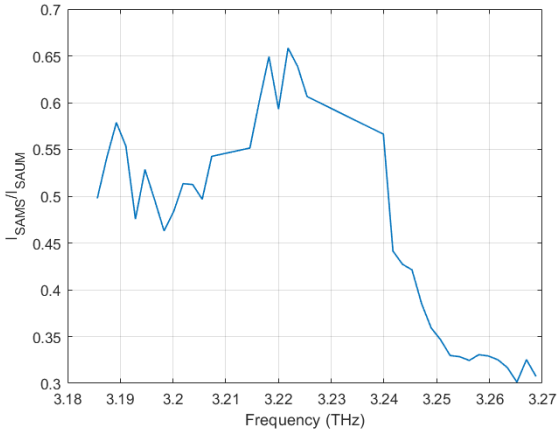

(b) Reflectance of sample using U-3.4-B1.

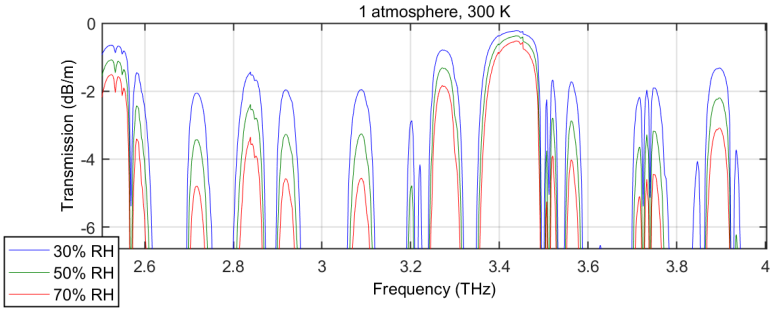

Figure 3.22: Atmospheric absorption data acquired from HITRAN.

Chapter 4

Conclusions and Future Work

In summary, I have expanded upon work inherited from my lab member Yu Wu, by performing simulations on and designing experiments to characterize our 3.4 THz metasurface saturable absorber samples. This involved performing preliminary experiments on a mid-IR sample to optimize alignment within the FTIR and externally, for the DW100 samples. As a result, I was able to:

1. Write scripts to calculate wavefunction distribution inside a QC active region, and use the results to estimate absorption coefficients.

2. Calculate the parameters required for the single-bounce transmission measurement of a mid-IR wedge sample, and derive the absorption coefficient of a mid-IR sample through this measurement. This was extended to designing an external transmission measurement system for the same sample.

3. Create a reflection-mode transmission measurement setup for THz samples using the experience from designing an external measurement setup for mid-IR samples, and use this setup to calculate the reflectance of a sample.

4. Confirm that our QC-VECSELs are capable of being used as spectroscopic sources to characterize samples in the terahertz.

My future work will require fabricating sources dedicated to the characterization of these and other saturable absorber samples, and extending our tests to biased saturable absorbers

cooled to cryogenic temperatures. At different points of the saturable absorber characterization, different QC-VECSEL sources were used. Some tested were not tunable near the saturable absorber resonance, while others suffered from reliability issues. In the future, QC-VECSELs will be designed explicitly for saturable absorber testing. To do so, I will continue to improve the alignment scheme for detection with the FTIR and with multiple pyroelectric detectors. When possible, I will repeat the reflectance measurements using a bolometer cooled to liquid He temperature (4K) and compare the results to the schemes included in this thesis. Later, I plan on designing an intra-cryostat mount to measure saturable absorption of a QC-VECSEL. My current work is two-pronged: I am improving the MATLAB scripts used to predict absorption behavior in our active regions, and I am also performing reflectance simulations involving both a quartz output coupler and a saturable absorber to estimate the output power of a beam reflected onto a saturable absorber after exiting the cavity:

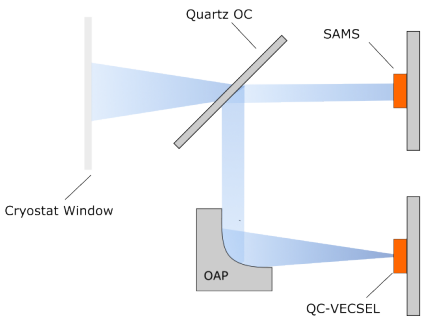

Figure 4.1: Intra-cryostat QC-VECSEL mode locking schematic.

Simulations of the output coupler and saturable absorber will inform the choice of intra-cryostat mounts and optics.

QC-VECSELs are promising sources for terahertz scpectroscopy, particularly in applications requiring a small footprint. Learning how to mode lock these lasers without external

electronics would not only make the technology more accessible, but also expand our understanding of complex carrier dynamics in QC structures.

REFERENCES

[1] David R. Bacon, Joshua R. Freeman, Reshma A. Mohandas, Lianhe Li, Edmund H. Linfield, A. Giles Davies, and Paul Dean. "Gain recovery time in a terahertz quantum cascade lasers". In: *Appl. Phys. Lett.* 108.8 (2015). DOI: https://doi.org/10.1063/1.4942452.

[2] Constantine A. Balanis. *Antenna Theory Analysis and Design, Fourth Ed.* Wiley, 2016. ISBN: 978-11186420601.

[3] *Beam Condensers*. 2021.

[4] COMSOL. *RF Module User's Guide*. 2017.

[5] John Creighton and Julius Jackson. "Simplified Theory of Picosecond Pulses in Lasers". In: *Journal of Applied Physics* 42.9 (1971), p. 3409. DOI: https://doi.org/10.1063/1.1660746.

[6] A. J. DeMaria, D. A. Stetser, and H. Heynau. "SELF MODE-LOCKING OF LASERS WITH SATURABLE ABSORBERS". In: *Appl. Phys. Lett.* 8.7 (1966), p. 174. DOI: https://doi.org/10.1063/1.1754541.

[7] Christian G. Demtl, Giacomo Scalari, Mattias Beck, Jérôme Faist, Karl Unterrainer, and Juraj Darmo. "Gain recovery dynamics in broadband terahertz quantum cascade lasers". In: *International Conference on Infrared, Millimeter, and Terahertz Waves* 43 (2018). DOI: 10.1109/IRMMW-THz.2018.8510275.

[8] M. Haiml, R. Grange, and U. Keller. "Optical characterization of semiconductor saturable absorbers". In: *Appl. Phys. B* 79 (2004), pp. 331–339. DOI: https://doi.org/10.1007/s00340-004-1535-1.

[9] Paul Harrison and Alex Valavanis. *Quantum Wells, Wires, and Dots*. Wiley, 2016. ISBN: 9781118923368.

[10] Hermann. A. Haus. "Theory of mode locking with a fast saturable absorber". In: *Journal of Applied Physics* 46.7 (1975), p. 3049. DOI: https://doi.org/10.1063/1.321997.

[11] Hermann. A. Haus. "Theory of mode locking with a slow saturable absorber". In: *IEEE Journal of Quantum Electronics* 11.9 (1975), pp. 736–746. DOI: 10.1109/JQE.1975.1068922.

[12] Johannes Hillbrand, Aaron Maxwell Andrews, Hermann Detz, Gottfried Strasser, and Benedikt Schwarz. "Coherent injection locking of quantum cascade laser frequency combs". In: *Nature Photonics* 13 (2017), pp. 101–104. DOI: https://doi.org/10.1038/s41566-018-0320-3.

[13] Christopher C. Homes, G. Lawrence Carr, Ricardo P. S. M. Lobo, Joseph D. LaVeigne, and David B. Tanner. "Silicon beam splitter for far-infrared and terahertz spectroscopy". In: *Applied Optics* 46 (32 2007), pp. 7884–7888. DOI: 10.1364/AO.46.007884.

[14] Philip W. C. Hon, Amir A. Tavallaee, Qi-Sheng Chen, Benjamin S. Williams, and Tatsuo Itoh. "Radiation Model for Terahertz Transmission-Line Metamaterial Quantum-Cascade Lasers". In: *IEEE Transactions on Terahertz Science and Technology* 2.3 (2012). DOI: 10.1109/TTHZ.2012.2191023.

[15] Christian Jirauschek and Tillmann Kubis. "Modeling techniques for quantum cascade lasers". In: *Applied Physics Reviews* 1.011307 (2014). DOI: 10.1063/1.4863665.

[16] U. Keller, K.J. Weingarten, F.X. Kartner, D. Kopf, B. Braun, I.D. Jung, R. Fluck, C. Honninger, N. Matuschek, and J Aus der Au. "Semiconductor saturable absorber mirrors (SESAM's) for femtosecond to nanosecond pulse generation in solid-state lasers". In: *IEEE Journal of Selected Topics in Quantum Electronics* 2.3 (1996). DOI: 10.1109/2944.571743.

[17] Ursula Keller. "Recent developments in compact ultrafast lasers". In: *Nature* 424 (2003), pp. 831–838.

[18] Ursula Keller and Anne C. Tropper. "Passively modelocked surface-emitting semiconductor lasers". In: *Physics Reports* 429 (2006), pp. 67–120. DOI: doi:10.1016/j.physrep.2006.03.004.

[19] K. Kurokawa. "Power Waves and the Scattering Matrix". In: *IEEE Transactions on Microwave Theory and Techniques* 13.2 (1965), pp. 194–202. DOI: 10.1109/TMTT.1965.1125964.

[20] Laman and Grischkowsky. "Terahertz conductivity of thin metal films". In: *Applied Physics Letters* 93 (5 2008). DOI: 10.1063/1.2968308.

[21] H.C. Liu and Federico Capasso. *Intersubband Transitions in Quantum Wells, Physics and Device Applications I*. Semiconductors and Semimetals. Academic Press, 2000. ISBN: 0-12-752171-2.

[22] Hans W. Mocker and R. J. Collins. "MODE COMPETITION AND SELF-LOCKING EFFECTS IN A Q-SWITCHED RUBY LASER". In: *Appl. Phys. Lett.* 7.10 (1965), p. 270. DOI: https://doi.org/10.1063/1.1754253.

[23] Dimitri Oustinov, Nathan Jukam, Rakchanok Rungsawang, Julien Madéo, Stefano Barbieri, Pascal Filloux, Carlo Sirtori, Xavier Marcadet, Jérôme Tignon, and Sukhdeep Dhillon. "Phase seeding of a terahertz quantum cascade laser". In: *Nature Communications* 1.69 (2010). DOI: https://doi.org/10.1038/ncomms1068.

[24] R. Paschotta and U. Keller. "Passive mode locking with slow saturable absorbers". In: *Appl. Phys. B* 73 (2001), pp. 653–662. DOI: 10.1007/s003400100726.

[25] Zhipeng Qin, Xuliang Chai, Guoqiang Xie, Zhicheng Xu, Yi Zhou, Qi Wu, Jie Li, Zhuan Wang, Yuxiang Weng, Ting Hai, Peng Yuan, Jingui Ma, Jianxin Chen, and Liejia Qian. "Semiconductor saturable absorber mirror in the 3–5 µm mid-infrared region". In: *Optics Letters* 47.4 (2022), pp. 890–893. DOI: 10.1364/OL.444485.

[26] J. Raab, Christoph Lange, Jessica L. Boland, Ignaz Laepple, Martin Furthmeier, Enrico Dardanis, Nils Dessmann, Lianhe Li, Edmund H. Linfield, A. Giles Davies, Miriam S. Vitiello, and Rupert Huber. "Ultrafast two-dimensional field spectroscopy of terahertz intersubband saturable absorbers". In: *Optics Express* 27.3 (2019). DOI: https://doi.org/10.1364/OE.27.002248.

[27] Jagdeep Shah. *Ultrafast Spectroscopy of Semiconductors and Semiconductor Nanostructures*. Springer Series in Solid-State Sciences. Springer-Verlag Berlin Heidelberg GmbH, 1999. ISBN: 978-3-642-08391-4. DOI: 10.1007/978-3-662-03770-6.

[28] Carlo Sirtori. "Bridge for the terahertz gap". In: *Nature* 417 (2002), pp. 132–133. DOI: https://doi.org/10.1038/417132b.

[29] B. H. Soffer. "Giant Pulse Laser Operation by a Passive, Reversibly Bleachable Absorber". In: *Journal of Applied Physics* 35.8 (1964), p. 2551. DOI: https://doi.org/10.1063/1.1702903.

[30] W.R. Sooy. "THE NATURAL SELECTION OF MODES IN A PASSIVE Q-SWITCHED LASER". In: *Appl. Phys. Lett.* 7.2 (1965), p. 36. DOI: https://doi.org/10.1063/1.1754286.

[31] P.P. Sorokin, J.J. Luzzi, J.R. Lankard, and G.D. Pettit. "Ruby Laser Q-Switching Elements Using Phthalocyanine Molecules in Solution". In: *IBM Journal* (1964), pp. 182–184.

[32] T. Chen Sverre, A. Turnbull, E. Mavrona P. Gow, J. R. C. Woods, C.R. Head, V. Apostolopoulos, and A. C. Tropper. "Mode-locked VECSEL SESAM with intracavity antenna for terahertz emission". In: *Proc. of SPIE* 10087 (2017). DOI: 10.1117/12.2252346.

[33] A. Szabo and R.A. Stein. "Theory of Laser Giant Pulsing by a Saturable Absorber". In: *Journal of Applied Physics* 36.5 (1965), p. 1562. DOI: https://doi.org/10.1063/1.1703087.

[34] William G. Wagner and Bela A. Lengyel. “Evolution of the Giant Pulse in a Laser”. In: *Journal of Applied Physics* 34.7 (1963), p. 2040. DOI: https://doi.org/10.1063/1.1729732.

[35] Benjamin S. Williams. “Terahertz quantum cascade lasers”. MIT, 2003.

[36] Luyao Xu, Christopher A. Curwen, Daguan Chen, John L. Reno, Tatsuo Itoh, and Benjamin S. Williams. “Terahertz Metasurface Quantum-Cascade VECSELs: Theory and Performance”. In: *IEEE Journal of Selected Topics in Quantum Electronics* 23.6 (2017). DOI: 10.1109/JSTQE.2017.2693024.